Commun. Comput. Phys.
doi: 10.4208/cicp.OA-2017-0178

Vol. **24**, No. 5, pp. 1523-1555
November 2018

# Application of the GRP Scheme for Cylindrical Compressible Fluid Flows

Rui Chen[1,2], Jiequan Li[2,3]* and Baolin Tian[2,3]

[1] *School of Science, Beijing University of Posts and Telecommunications, Beijing 100876, P.R. China.*
[2] *Institute of Applied Physics and Computational Mathematics, Beijing 100088, P.R. China.*
[3] *Center for Applied Physics and Technology, Peking University, Beijing, P.R. China.*

Communicated by Kun Xu

Received 21 August 2017; Accepted (in revised version) 17 November 2017

**Abstract.** This paper contributes to apply both the direct Eulerian and Lagrangian generalized Riemann problem (GRP) schemes for the simulation of compressible fluid flows in two-dimensional cylindrical geometry. Particular attention is paid to the treatment of numerical boundary conditions at the symmetric center besides the zero velocity (momentum) enforced by the symmetry. The new treatment precisely describes how the thermodynamical variables are discretized near the center using the conservation property. Moreover, the Lagrangian GRP scheme is verified rigorously to satisfy the properties of symmetry and conservation. Numerical results demonstrate the performance of such treatments and the symmetry preserving property of the scheme with second order accuracy both in space and time.

**AMS subject classifications**: 65M08, 76N15, 76L05, 76M12

**Key words**: Euler equations, cylindrical geometry, the generalized Riemann problem (GRP) scheme.

## 1 Introduction

The simulation of compressible fluid flows in cylindrical symmetric geometry has been received great attention due to practical demands [2, 10, 11] and numerical difficulties as shown in [1, 6, 12, 16–18, 24, 35, 36]. The difficulties lie in the prevention of wall-heating phenomenon near the center [31], the alleviation of the large distortion of Lagrangian mesh [33], the symmetry and positivity preserving [16–18, 35], and the conservation of

---

*Corresponding author. *Email addresses:* `ruichen@bupt.edu.cn` (R. Chen), `li_jiequan@iapcm.ac.cn` (J. Li), `Tian_baolin@iapcm.ac.cn` (B. Tian)

momentum and total energy [28] etc, besides the accuracy requirement [30]. There are quite a few works about this issue in literature. For example, in [16] Cheng and Shu propose a cell-centered Lagrangian scheme with preservation of symmetry and conservation properties, using an equal-angle-zoned initial grid. The area-weighted method is widely used in spherical symmetry preservation in two-dimensional cylindrical coordinates with the sacrifice of strict momentum and total energy conservation [14,28]. In [35,36], V*á*chal and Wendroff study a staggered grid Lagrangian scheme to maintain spherical symmetry exactly on an qual-angle-zoned grid. For numerical boundary conditions at the symmetric center, people mostly set zero velocity and use a symmetric extension for thermodynamical variables by using the property of symmetry [16,35,36], in addition that the conservation laws are adopted to derive the boundary conditions for spherical cases in [24]. High order WENO type methods are also available [30].

This paper applies the generalized Riemann problem (GRP) solver both in the Eulerian and Lagrangian versions to simulate the cylindrical compressible fluid flows [9,24]. The GRP solver, a second order temporal-spatial coupled Godunov-type solver, was originally derived in [5] and has been applied extensively since then. This paper contributes the following: (1) The method in [24] is extended for the cylindrical case to derive the boundary condition at the symmetrical center both theoretically and numerically. This newly derived boundary conditions are consistent with the conservation laws of mass, momentum and energy. (2) The geometrical source term is discretized using an interface method [8], for which the interface values by the GRP solver are adopted together with the numerical flux approximation. Such a discretization can keep the well-balancing property, as shown in [8] besides the algorithm simplicity. (3) The symmetry property is automatically preserved due to the feature of the GRP scheme, which is verified rigorously by using the almost the same approach as in [16]. The resulting scheme could be useful even in the study of flow transition problems [15,21,22].

We organize this paper as follows. In Section 2, the compressible Euler equations are described both in cylindrical coordinate and local coordinate, the direct Eulerian GRP scheme is given over equal angular polar grid, and the data reconstruction is provided, including gradient computing and limiter constraints. In Section 3, the numerical boundary conditions at the center are derived. In Section 4, we construct a Lagrangian GRP scheme with the symmetry and conservation properties for Euler equations in cylindrical coordinates, and give the numerical boundary condition at the center in Lagrangian formulation. We carry out several numerical examples in Section 5 to demonstrate the accuracy, the efficiency and the performance of the two types of GRP schemes, and the effectiveness of the numerical boundary condition at the center.

## 2 The GRP scheme for 2-D cylindrical Euler flows

As is well known, the compressible Euler equations in two-dimensional cylindrical geometry are written in the form,

$$(r\mathbf{U})_t+(r\mathbf{F}(\mathbf{U}))_z+(r\mathbf{G}(\mathbf{U}))_r=\mathbf{\Psi}(\mathbf{U}), \tag{2.1}$$

with

$$\begin{aligned}
&\mathbf{U}=\begin{bmatrix}\rho\\ \rho u\\ \rho v\\ \rho E\end{bmatrix}, \quad \mathbf{F}(\mathbf{U})=\begin{bmatrix}\rho u\\ \rho u^2+p\\ \rho uv\\ u(\rho E+p)\end{bmatrix}, \quad \mathbf{G}(\mathbf{U})=\begin{bmatrix}\rho v\\ \rho uv\\ \rho v^2+p\\ v(\rho E+p)\end{bmatrix},\\
&\mathbf{\Psi}(\mathbf{U})=\begin{bmatrix}0\\ 0\\ p\\ 0\end{bmatrix},
\end{aligned} \tag{2.2}$$

where $z$ and $r$ are the axial and radial directions respectively, the total energy $E=e+(u^2+v^2)/2$, the variables $\rho$, $p$, $e$, $u$, $v$ are density, pressure, internal energy, velocity components in the $z$ and $r$ directions, respectively. The geometrical source term $\mathbf{\Psi}(U)$ results from the transformation from the Cartesian coordinates to the radially symmetric coordinates. This system (2.1) is closed by the equation of state (EOS) $p=p(\rho,e)$. For polytropic gases, the equation of state has a simple form $p=(\gamma-1)\rho e$, where $\gamma>1$ is a constant representing the ratio of specific heat capacities of the fluid.

We follow the notations in [16] and are concerned with the cylindrical geometry $(z,r)$, as indicated in Fig. 1, which shows an equal-angle-zone grid with $k$- lines radially outward and $\ell$- lines in angular direction. For such an equal-angle-zone grid, the cell has the property that the angles between $\xi$ and the two equal sides of the cell are the same, where $\xi$ is the radial direction passing through the cell center and the origin, and $\theta$ is the angular direction orthogonal to $\xi$. To perform this local coordinate transformation in each cell, the Euler equations in cylindrical coordinates (2.1) are rewritten in the following form

$$(\xi^2\tilde{\mathbf{U}})_t+(\xi^2\mathbf{F}(\tilde{\mathbf{U}}))_\xi+(\xi^2\mathbf{G}(\tilde{\mathbf{U}}))_\theta=\mathbf{\Psi}(\tilde{\mathbf{U}}), \tag{2.3}$$

with

$$\begin{aligned}
&\tilde{\mathbf{U}}=\begin{bmatrix}\rho\\ \rho u_\xi\\ \rho u_\theta\\ \rho E\end{bmatrix}, \quad \mathbf{F}(\tilde{\mathbf{U}})=\begin{bmatrix}\rho u_\xi\\ \rho(u_\xi)^2+p\\ \rho u_\xi u_\theta\\ u_\xi(\rho E+p)\end{bmatrix}, \quad \mathbf{G}(\tilde{\mathbf{U}})=\begin{bmatrix}\rho u_\theta\\ \rho u_\xi u_\theta\\ \rho(u_\theta)^2+p\\ u_\theta(\rho E+p)\end{bmatrix},\\
&\mathbf{\Psi}(\tilde{\mathbf{U}})=2\xi\begin{bmatrix}0\\ p\\ 0\\ 0\end{bmatrix},
\end{aligned} \tag{2.4}$$

where the coordinate transformation is

$$r=\xi\sin\theta, \quad z=\xi\cos\theta. \tag{2.5}$$

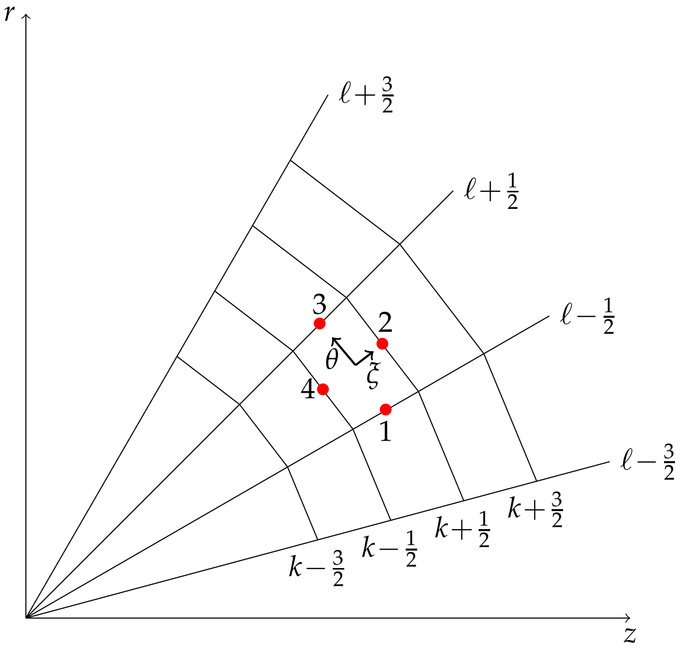

Figure 1: The equal-angle-zone grid.

Thus we obtain the Euler equations in spherical coordinate form.

The two-dimensional spatial domain $\Omega$ is discretized into $K\times L$ quadrilateral cells $I_{k,\ell}$. The four vertices of $I_{k,\ell}$ are $(z_{k-1/2,\ell-1/2},r_{k-1/2,\ell-1/2})$, $(z_{k+1/2,\ell-1/2},r_{k+1/2,\ell-1/2})$, $(z_{k+1/2,\ell+1/2},\ r_{k+1/2,\ell+1/2})$ and $(z_{k-1/2,\ell+1/2},r_{k-1/2,\ell+1/2})$ when $k>1$, or triangular cells around the center ($k=1$). Denote by $V_{k,\ell}$ the volume of the cell $I_{k,\ell}$. Assume that a partition of the time interval $[0,T]$ is given as $\{t_{n+1}=t_n+\Delta t_n;t_0=0,\Delta t_n>0,n\in\mathbb{N}\}$, with the time step size $\Delta t_n$ determined by the stability condition in practice, and denote by a control volume $C_{k,\ell}=I_{k,\ell}\times[t_n,t_{n+1})$ with $m$ lateral faces $A^j_{k,\ell}$ shown in Fig. 2, where $m=3$ or 4 and $j=1,\cdots,m$. The boundary of $I_{k,\ell}$ is $l^j_{k,\ell}$, $j=1,\cdots,m$. The neighbor cells of $I_{k,\ell}$ are $\{I^j_{k,\ell},j=1,2,3,4\}$ when $1<k<K$, $1<\ell<L$. $\mathbf{x}^c_{k,\ell}=(z,r)^c_{k,\ell}$, $\mathbf{x}^j_{k,\ell}=(z,r)^j_{k,\ell}$ are the center points of the cell $I_{k,\ell}$ and the side $l^j_{k,\ell}$, respectively.

In the framework of cell-centered scheme in the finite volume method, all the variables are stored as cell averages at the cell center of $I_{k,\ell}$,

$$\bar{U}^n_{k,\ell}=\frac{1}{V_{k,\ell}}\int_{I_{k,\ell}}\bar{U}(\xi,\theta,t_n)\xi^2d\xi d\theta,\quad \bar{U}=(\bar{\rho},\overline{\rho u_\xi},\overline{\rho u_\theta},\overline{\rho E})^\top,\quad V_{k,\ell}=\int_{I_{k,\ell}}\xi^2d\xi d\theta. \tag{2.6}$$

We write (2.3) over the control volume $C_{k,\ell}$ as

$$\bar{U}^{n+1}_{k,\ell}=\bar{U}^n_{k,\ell}-\frac{1}{V_{k,\ell}}\sum_{j=1}^{m}\int_{A^j_{k,\ell}}\mathcal{F}(\tilde{\mathbf{U}})\cdot\mathbf{n}^j_{k,\ell}dS+\frac{1}{V_{k,\ell}}\int_{C_{k,\ell}}\mathbf{\Psi}(\tilde{\mathbf{U}})d\xi d\theta dt,\quad m=3\text{ or }4, \tag{2.7}$$

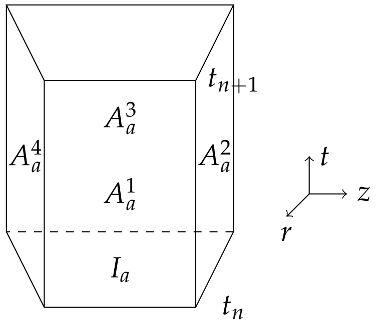

Figure 2: The control volume $C_a$ $(a=(k,\ell))$.

where $\mathcal{F}=\xi^2(\mathbf{F}(\tilde{\mathbf{U}}),\mathbf{G}(\tilde{\mathbf{U}}))$, $\mathbf{x}=(z,r)$, and $\mathbf{n}^j_{k,\ell}$ is the unit outward normal vector of the boundary $l^j_{k,\ell}$. Assume that the data at time $t=t_n$ is piecewise linear

$$\tilde{\mathbf{U}}(\mathbf{x},t_n)=\bar{U}^n_{k,\ell}+\boldsymbol{\oe}^n_{k,\ell}\cdot(\mathbf{x}-\mathbf{x}_{k,\ell}),\quad \mathbf{x}\in I_{k+\frac{1}{2},\ell+\frac{1}{2}}, \tag{2.8}$$

in which $\boldsymbol{\oe}^n_{k,\ell}$ is the gradient of $\tilde{\mathbf{U}}$ in the cell $I_{k,\ell}$. Using the mid-point rule, the numerical flux through $A^j_{k,\ell}$ in (2.7) is approximated as

$$\int_{A^j_{k,\ell}}\mathcal{F}(\tilde{\mathbf{U}})\cdot\mathbf{n}^j_{k,\ell}dS\approx\mathcal{F}(\tilde{\mathbf{U}}^{n+\frac{1}{2}}_{A^j_{k,\ell}})\cdot\mathbf{n}^j_{k,\ell}|A^j_{k,\ell}|, \tag{2.9}$$

where $|A^j_{k,\ell}|=|l^j_{k,\ell}|\Delta t_n$ is the area of $A^j_{k,\ell}$, and $|l^j_{k,\ell}|$ is the length of side $l^j_{k,\ell}$. The value $\tilde{\mathbf{U}}^{n+\frac{1}{2}}_{A^j_{k,\ell}}$ is defined in the center of $A^j_{k,\ell}$. The source term in (2.7) is approximated as follows

$$\frac{1}{V_{k,\ell}}\int_{C_{k,\ell}}\mathbf{\Psi}(\tilde{\mathbf{U}})d\mathbf{x}dt\approx\frac{\Delta t_n}{m}\sum_{j=1}^{m}\mathbf{\Psi}(\tilde{\mathbf{U}}^{n+\frac{1}{2}}_{A^j_{k,\ell}}),\quad m=3\text{ or }4, \tag{2.10}$$

using the interface method [8].

## 2.1 The generalized Riemann problem (GRP) solver

Now we use the generalized Riemann problem (GRP) solver to approximate the value $\tilde{\mathbf{U}}^{n+\frac{1}{2}}_{A^j_{k,\ell}}$ by solving the following generalized Riemann problem [7,9,25] in the normal direction,

$$\begin{cases} \frac{\partial\tilde{\mathbf{U}}}{\partial t}+\frac{\partial}{\partial\eta}\mathcal{H}(\tilde{\mathbf{U}};\mathbf{n}^j_{k,\ell})=S(\tilde{\mathbf{U}}),\quad \mathcal{H}=(\mathbf{F},\mathbf{G})\cdot\mathbf{n}^j_{k,\ell}, \\ \tilde{\mathbf{U}}(\eta,0)=\begin{cases}\tilde{\mathbf{U}}_{\bar{L}}+\eta\tilde{\mathbf{U}}'_{\eta\bar{L}}, & \eta<0,\\ \tilde{\mathbf{U}}_R+\eta\tilde{\mathbf{U}}'_{\eta R}, & \eta>0,\end{cases} \end{cases} \tag{2.11}$$

where $\eta=\mathbf{x}\cdot\mathbf{n}^j_{k,\ell}$, $S(\tilde{\mathbf{U}})$ is the source term, the notations $\tilde{\mathbf{U}}_{\bar{L}}$, $\tilde{\mathbf{U}}_R$, $\tilde{\mathbf{U}}'_{\eta\bar{L}}$, and $\tilde{\mathbf{U}}'_{\eta R}$ are

$$\left\{\begin{array}{l}\tilde{\mathbf{U}}_{\bar{L}}=\tilde{\mathbf{U}}_{I_{k,\ell}}(\mathbf{x}^j_{k,\ell},t_n),\\ \tilde{\mathbf{U}}_R=\tilde{\mathbf{U}}_{I^j_{k,\ell}}(\mathbf{x}^j_{k,\ell},t_n),\end{array}\right. \qquad \left\{\begin{array}{l}\tilde{\mathbf{U}}'_{\eta\bar{L}}=\boldsymbol{\oe}^n_{k,\ell}\cdot\mathbf{n}^j_{k,\ell},\\ \tilde{\mathbf{U}}'_{\eta R}=\boldsymbol{\oe}^{j,n}_{k,\ell}\cdot\mathbf{n}^j_{k,\ell}.\end{array}\right. \tag{2.12}$$

With the standard Riemann solver [34], we obtain the value $\tilde{\mathbf{U}}^n_{A^j_{k,\ell}}$. The GRP solver serves to obtain $(\partial\tilde{\mathbf{U}}/\partial t)^n_{A^j_{k,\ell}}$. Once these values are available, we can immediately define a "centroid" value on the interface $A^j_{k,\ell}$ with the formula

$$\tilde{\mathbf{U}}^{n+\frac{1}{2}}_{A^j_{k,\ell}}=\tilde{\mathbf{U}}^n_{A^j_{k,\ell}}+\frac{\Delta t_n}{2}\left(\frac{\partial\tilde{\mathbf{U}}}{\partial t}\right)^n_{A^j_{k,\ell}}, \tag{2.13}$$

which is used in numerical flux (2.9) and source term (2.10). Thus we can implement the GRP scheme in the following three steps.

**Step 1.** Given piecewise linear initial data (2.8), calculate the centroid value $\tilde{\mathbf{U}}^{n+\frac{1}{2}}_{A^j_{k,\ell}}$ for each cell $I_{k,\ell}$ with formula (2.13) by solving the local generalized Riemann problem (2.11).

**Step 2.** Evaluate the new cell averages $\bar{U}^{n+1}_{k,\ell}$ using (2.7), (2.9), and (2.10).

**Step 3.** Update the gradient $\boldsymbol{\oe}^{n+1}_{k,\ell}$ with a monotonicity algorithm-slope limiter that will be introduced in the next Subsection.

## 2.2 Data reconstruction

In the finite volume framework, the data reconstruction is a necessary step to obtain cellwise polynomials with desired accuracy. If the structural meshes are preferred, the gradients can be updated together with the solution in the framework of the GRP methodology. However, the cell $I_{k,\ell}$ is unstructured in coordinate $(z,r)$ in Fig. 1. There are various methods, such as (weighted) least squares method [25,29], Green-Gauss method [3] and multislope method [13], to compute the gradients $\boldsymbol{\oe}^{n+1}_{k,\ell}$. In the current study, we adopt the following method.

Note that the gradient $\boldsymbol{\oe}^{n+1}_{k,\ell}$ is in symmetry at the local $\xi$ axis, thus we compute the gradient $(q_\xi,q_\theta)_{k,\ell}$ of a physical variable $q$ in local coordinate $(\xi,\theta)$. Firstly, we obtain the value of the physical variable at each side of cell by the GRP solver and the Riemann solver

$$\tilde{\mathbf{U}}^{n+1,-}_{A^j_{k,\ell}}=\tilde{\mathbf{U}}^n_{A^j_{k,\ell}}+\Delta t_n\left(\frac{\partial\tilde{\mathbf{U}}}{\partial t}\right)^n_{A^j_{k,\ell}}, \quad j=1,\cdots,4. \tag{2.14}$$

Then we can obtain the gradient of data over $I_{k,\ell}$ in local coordinate $(\xi,\theta)$ approximately (see Fig. 1),

$$\mathbf{œ}_{k,\ell}^{n+1,-}=(\tilde{\mathbf{U}}_{\xi},\tilde{\mathbf{U}}_{\theta})_{k,\ell}^{n+1,-}\approx\left(\frac{\tilde{\mathbf{U}}^{n+1,-}_{A^2_{k,\ell}}-\tilde{\mathbf{U}}^{n+1,-}_{A^4_{k,\ell}}}{||\mathbf{x}^2_{k,\ell}-\mathbf{x}^4_{k,\ell}||},\frac{\tilde{\mathbf{U}}^{n+1,-}_{A^3_{k,\ell}}-\tilde{\mathbf{U}}^{n+1,-}_{A^1_{k,\ell}}}{||\mathbf{x}^3_{k,\ell}-\mathbf{x}^1_{k,\ell}||}\right). \tag{2.15}$$

In order to suppress local oscillations near discontinuities, we need some limiters to correct the gradients $\mathbf{œ}_{k,\ell}^{n+1,-}$. Here we adopt a monotonicity algorithm-slope limiter to implement on $\mathbf{œ}_{k,\ell}^{n+1,-}$,

$$\begin{aligned}
(\tilde{\mathbf{U}}_{\xi})_{k,\ell}^{n+1}&=\text{minmod}\left(\alpha\frac{\tilde{\mathbf{U}}^{n+1}_{k,\ell}-\tilde{\mathbf{U}}^{n+1}_{k-1,\ell}}{||\mathbf{x}^c_{k,\ell}-\mathbf{x}^{c,}_{k-1,\ell}||},(\tilde{\mathbf{U}}_{\xi})_{k,\ell}^{n+1,-},\alpha\frac{\tilde{\mathbf{U}}^{n+1}_{k+1,\ell}-\tilde{\mathbf{U}}^{n+1}_{k,\ell}}{||\mathbf{x}^c_{k+1,\ell}-\mathbf{x}^{c,}_{k,\ell}||}\right),\\
(\tilde{\mathbf{U}}_{\theta})_{k,\ell}^{n+1}&=\text{minmod}\left(\alpha\frac{\tilde{\mathbf{U}}^{n+1}_{k,\ell}-\tilde{\mathbf{U}}^{n+1}_{k,\ell-1}}{||\mathbf{x}^c_{k,\ell}-\mathbf{x}^{c,}_{k,\ell-1}||},(\tilde{\mathbf{U}}_{\theta})_{k,\ell}^{n+1,-},\alpha\frac{\tilde{\mathbf{U}}^{n+1}_{k,\ell+1}-\tilde{\mathbf{U}}^{n+1}_{k,\ell}}{||\mathbf{x}^c_{k,\ell+1}-\mathbf{x}^{c,}_{k,\ell}||}\right),\\
\mathbf{œ}_{k,\ell}^{n+1}&=\left(\tilde{\mathbf{U}}_{\xi},\tilde{\mathbf{U}}_{\theta}\right)_{k,\ell}^{n+1},
\end{aligned} \tag{2.16}$$

with the parameter $\alpha\in[0,2)$. This monotonicity algorithm corresponds a non-sawtooth case for $\alpha\in[0,1]$ and a sawtooth case for $\alpha\in(1,2)$. In our scheme, $\alpha$ is taken in $[1.5,2)$, and the minmod function can be found in [5,19].

**Remark 2.1.** It must be careful to compute the gradient for the cell near the boundary. That is, there is at least one side of the cell along the boundary. As $\ell=1$ or $\ell=L$, we have

$$\mathbf{œ}_{k,1}^{n+1}=\mathbf{œ}_{k,2}^{n+1},\quad \mathbf{œ}_{k,\ell}^{n+1}=\mathbf{œ}_{k,\ell-1}^{n+1},\quad k=2,\cdots,K-1. \tag{2.17}$$

When $k=K$, we also have

$$\mathbf{œ}_{k,\ell}^{n+1}=\mathbf{œ}_{K-1,\ell}^{n+1},\quad \ell=1,\cdots,L. \tag{2.18}$$

When $k=1$, we let

$$\begin{aligned}
&(\tilde{\mathbf{U}}_{\xi})_{1,\ell}^{n+1}=\text{minmod}\left(\alpha\frac{\tilde{\mathbf{U}}^{n+1,-}_{A^2_{1,\ell}}-\tilde{\mathbf{U}}^{n+1}_{1,\ell}}{||\mathbf{x}^2_{1,\ell}-\mathbf{x}_{1,\ell}||},(\tilde{\mathbf{U}}_{\xi})_{2,\ell}^{n+1}\right),\\
&(\tilde{\mathbf{U}}_{\theta})_{1,\ell}^{n+1}=(\tilde{\mathbf{U}}_{\theta})_{2,\ell}^{n+1},\quad \sigma_{1,\ell}^{n+1}=\left(\tilde{\mathbf{U}}_{\xi},\tilde{\mathbf{U}}_{\theta}\right)_{1,\ell}^{n+1},\quad \ell=1,\cdots,L.
\end{aligned} \tag{2.19}$$

## 3 Boundary conditions at the symmetry center

We use the transmission boundary condition at the $\theta$-direction boundary

$$\tilde{\mathbf{U}}_{k,1}^{n+1}=\tilde{\mathbf{U}}_{k,2}^{n+1},\quad \tilde{\mathbf{U}}_{k,\ell}^{n+1}=\tilde{\mathbf{U}}_{k,\ell-1}^{n+1},\quad k=2,\cdots,K-1, \tag{3.1}$$

and the outer boundary

$$\tilde{\mathbf{U}}^{n+1}_{K,\ell}=\tilde{\mathbf{U}}^{n+1}_{K-1,\ell}, \quad \ell=1,\cdots,L. \tag{3.2}$$

However, there are two major difficulties for the boundary at the center $(z,r)=(0,0)$. One is the numerical boundary condition, and the other is the singular nature proportional to $1/\xi$. The latter is relatively easy to deal with such as the CFL restriction, or an implicit strategy, even or a weighted average strategy [30]. The former is more inherent and a common strategy is to set zero velocity and exert an extension of thermodynamical variables symmetrically. In the current study, we extend the method in [26] to deal with the boundary condition at the symmetry center. We will theoretically derive such a boundary condition in the following proposition.

**Proposition 3.1.** For the cylindrical symmetric flow, at the symmetry center $r=0$, the velocity component in the $r$ direction must vanish, i.e. $v(0,z,t)\equiv 0$. The mass and total energy satisfy

$$\begin{aligned}
&\Big(\frac{\partial \rho}{\partial t}\Big)_0+2\Big(\frac{\partial(\rho v)}{\partial r}\Big)_0+\Big(\frac{\partial(\rho u)}{\partial z}\Big)_0=0,\\
&\Big(\frac{\partial(\rho E)}{\partial t}\Big)_0+2\Big(\frac{\partial(\rho E+p)v}{\partial r}\Big)_0+\Big(\frac{\partial(\rho E+p)u}{\partial z}\Big)_0=0,
\end{aligned} \tag{3.3}$$

and the momentum satisfy

$$\begin{aligned}
&\Big(\frac{\partial(\rho u_\xi)}{\partial t}\Big)_0+2\Big(\frac{\partial(\rho uv)}{\partial r}\Big)_0+\Big(\frac{\partial(\rho u^2+p)}{\partial z}\Big)_0=0,\\
&\Big(\frac{\partial(\rho v)}{\partial t}\Big)_0+2\Big(\frac{\partial(\rho v^2)}{\partial r}\Big)_0+\Big(\frac{\partial(\rho uv)}{\partial z}\Big)_0=0,
\end{aligned} \tag{3.4}$$

provided that the flow is smooth, where the subscript 0 stands for the flow state at the center.

*Proof.* According to the symmetry of cylindrical flow, the velocity component in the $r$ direction at the center $r=0$ must be zero.

The mass conservative law for any domain $\Omega$ can be written as,

$$\frac{\partial}{\partial t}\int_\Omega \rho dV+\int_{\partial\Omega}\rho\vec{v}\cdot\vec{n}dS=0, \tag{3.5}$$

where $\vec{v}$ is the velocity vector, $\vec{n}$ is the outward unit vector pertaining to the domain boundary $\partial\Omega$. For a cylindrical symmetric flow, $\Omega$ is taken as a cylinder of a radius $\Delta r$ centered at the origin. With the cylindrical coordinate transformation, (3.5) can be rewritten as

$$\int_0^{2\pi}\int_0^{\Delta r} r\frac{\partial\rho}{\partial t}drd\phi+\int_0^{2\pi}\Delta r\rho v(\Delta r,z,t)d\phi+\int_0^{2\pi}\int_0^{\Delta r}(r\rho u)_z drd\phi=0. \tag{3.6}$$

Using the mean value theorem of integration, the above equation can be reduced to

$$\frac{\partial\rho(\tilde{b}\Delta r,z,t)}{\partial t}+2\frac{\rho v(\Delta r,z,\theta,t)}{\Delta r}+\frac{\partial\rho u(\tilde{c}\Delta r,z,t)}{\partial z}=0, \tag{3.7}$$

where $\tilde{b}$, $\tilde{c}\in[0,1]$. Sending $\Delta r$ to zero yields the first equation in (3.3). The same argument applies for the energy equation to yields the second identity in (3.3).

For the momentum equation, we have

$$\frac{d}{dt}\int_{\Omega}\rho\vec{v}dV+\int_{\partial\Omega}(\rho\vec{v}\otimes\vec{v}+pI)\vec{n}dS=\vec{0}.$$

For a cylindrical flow, with the cylindrical transformation, and with the symmetry argument, the above equation can be rewritten as

$$\begin{aligned}\int_0^{2\pi}\int_0^{\Delta r} r\frac{\partial(\rho u)}{\partial t}drd\phi+\int_0^{2\pi}\Delta r\rho uv(\Delta r,z,t)d\phi&\\ +\int_0^{2\pi}\int_0^{\Delta r} r(\rho u^2+p)_z drd\phi=0,&\end{aligned} \tag{3.8}$$

$$\begin{aligned}\int_0^{2\pi}\int_0^{\Delta r} r\frac{\partial(\rho v)}{\partial t}drd\phi+\int_0^{2\pi}\Delta r(\rho v^2+p)(\Delta r,z,t)d\phi&\\ +\int_0^{2\pi}\int_0^{\Delta r} r(\rho uv)_z drd\phi=\int_0^{2\pi}\int_0^{\Delta r} pdrd\phi.&\end{aligned} \tag{3.9}$$

Using the mean value theorem of integration, we have

$$\frac{\partial\rho u(\tilde{b}_1\Delta r,z,t)}{\partial t}+2\frac{\rho uv(\Delta r,z,t)}{\Delta r}+\frac{\partial(\rho u^2+p)(\tilde{c}_1\Delta r,z,t)}{\partial z}=0, \tag{3.10}$$

$$\frac{\partial\rho v(\tilde{b}_2\Delta r,z,t)}{\partial t}+2\frac{(\rho v^2+p)(\Delta r,z,t)}{\Delta r}+\frac{\partial(\rho uv)(\tilde{c}_2\Delta r,z,t)}{\partial z}=\frac{2}{\Delta r}p(\tilde{d}_2\Delta r,z,t), \tag{3.11}$$

where $\tilde{b}_1$, $\tilde{b}_2$, $\tilde{c}_1$, $\tilde{c}_2$, $\tilde{d}_2\in[0,1]$. Sending $\Delta r$ to zero yields the two equations (3.4). ☐

When the cylindrical form (2.1) is transformed to the spherical form (2.3), the boundary conditions must satisfy the flowing proposition.

**Proposition 3.2.** For the spherical symmetric flow, at the symmetry center $(z,r)=(0,0)$ (or $(\xi,\theta)=(0,\theta)$), the velocity must vanish, i.e. $u_\xi(0,\theta,t)\equiv 0$, $u_\theta(0,\theta,t)\equiv 0$. The mass and total energy satisfy

$$\Big(\frac{\partial\rho}{\partial t}\Big)_0+3\Big(\frac{\partial(\rho u_\xi)}{\partial\xi}\Big)_0=0,\quad \Big(\frac{\partial(\rho E)}{\partial t}\Big)_0+3\Big(\frac{\partial(\rho E+p)u_\xi}{\partial\xi}\Big)_0=0, \tag{3.12}$$

and the momentum satisfy

$$\Big(\frac{\partial(\rho u_\xi)}{\partial t}\Big)_0+3\Big(\frac{\partial(\rho u_\xi^2)}{\partial\xi}\Big)_0=0,\quad \Big(\frac{\partial(\rho u_\theta)}{\partial t}\Big)_0+3\Big(\frac{\partial(\rho u_\xi u_\theta)}{\partial\xi}\Big)_0=0, \tag{3.13}$$

provided that the flow is smooth, where the subscript 0 stands for the flow state at the center.

*Proof.* According to the symmetry of spherical flow, the velocity at the center must be zero.

The mass conservative law for any domain $\Omega$ can be written as,

$$\frac{\partial}{\partial t}\int_{\Omega}\rho dV+\int_{\partial\Omega}\rho\vec{v}\cdot\vec{n}dS=0, \tag{3.14}$$

where $\vec{v}$ is the velocity vector, $\vec{n}$ is the outward unit vector pertaining to the domain boundary $\partial\Omega$. For a spherical symmetric flow, $\Omega$ is taken as a sphere of a radius $\Delta\xi$ centered at the origin. With the spherical coordinate transformation, (3.14) can be rewritten as

$$\int_0^{2\pi}d\phi\int_0^{\pi}\int_0^{\Delta\xi}\xi^2\sin\theta\frac{\partial\rho}{\partial t}d\xi d\theta+\int_0^{2\pi}d\phi\int_0^{\pi}(\Delta\xi)^2\sin\theta\rho u_{\xi}(\Delta\xi,\theta,t)d\theta=0. \tag{3.15}$$

Using the mean value theorem of integration, the above equation can be reduced to

$$\frac{\partial\rho(b\Delta\xi,\theta,t)}{\partial t}+3\frac{\rho u_{\xi}(\Delta\xi,\theta,t)}{\Delta\xi}=0, \tag{3.16}$$

where $b\in[0,1]$. Sending $\Delta\xi$ to zero yields the first equation in (3.12). The same argument applies for the energy equation to yields the second identity in (3.12).

For the momentum equation, we have

$$\frac{d}{dt}\int_{\Omega}\rho\vec{v}dV+\int_{\partial\Omega}(\rho\vec{v}\otimes\vec{v}+pI)\vec{n}dS=\vec{0}.$$

For a spherical flow, with the spherical transformation, and with the symmetry argument, the above equation can be rewritten as

$$\begin{aligned}&\int_0^{2\pi}d\phi\int_0^{\pi}\int_0^{\Delta\xi}\xi^2\sin\theta\frac{\partial(\rho u_{\xi})}{\partial t}d\xi d\theta+\int_0^{2\pi}d\phi\int_0^{\pi}\Delta\xi^2\sin\theta\rho(u_{\xi})^2(\Delta\xi,\theta,t)d\theta\\ =&\int_0^{2\pi}d\phi\int_0^{\pi}\left(\int_0^{\Delta\xi}2\xi p\sin\theta d\xi-\Delta\xi^2\sin\theta p\right)d\theta, \end{aligned}\tag{3.17}$$

$$\begin{aligned}&\int_0^{2\pi}d\phi\int_0^{\pi}\int_0^{\Delta\xi}\xi^2\sin\theta\frac{\partial(\rho u_{\theta})}{\partial t}d\xi d\theta+\int_0^{2\pi}d\phi\int_0^{\pi}\Delta\xi^2\sin\theta\rho(u_{\xi}u_{\theta})(\Delta\xi,\theta,t)d\theta\\ =&0.\end{aligned}\tag{3.18}$$

Using the mean value theorem of integration, we have

$$\frac{\partial\rho u_{\xi}(b_1\Delta\xi,\theta,t)}{\partial t}+3\frac{\rho u_{\xi}^2(\Delta\xi,\theta,t)}{\Delta\xi}=0, \tag{3.19}$$

$$\frac{\partial\rho u_{\theta}(b_2\Delta\xi,\theta,t)}{\partial t}+3\frac{\rho u_{\xi}u_{\theta}(\Delta\xi,\theta,t)}{\Delta\xi}=0, \tag{3.20}$$

where $b_1,b_2\in[0,1]$. Sending $\Delta\xi$ to zero yields the two equations (3.13). ☐

**Proposition 3.3.** For the spherical symmetric flow, the numerical boundary condition $U_{1,\ell}^{n+1}=(\rho,\rho u_\xi,\rho u_\theta,\rho E)_{1,\ell}^{n+1}$ at the center can be expressed as follows

$$\begin{aligned}
&\rho_{1,\ell}^{n+1}=\rho_{1,\ell}^{n}-3\cdot\frac{\Delta t_n}{||\mathbf{x}_{1,\ell}^2||}(\rho u_\xi)_{A_{1,\ell}^2}^{n+\frac{1}{2}},\\
&(\rho u_\xi)_{1,\ell}^{n+1}=(\rho u_\xi)_{1,\ell}^{n}-3\cdot\frac{\Delta t_n}{||\mathbf{x}_{1,\ell}^2||}(\rho u_\xi^2)_{A_{1,\ell}^2}^{n+\frac{1}{2}},\\
&(\rho u_\theta)_{1,\ell}^{n+1}=\rho u_\theta)_{1,\ell}^{n}-3\cdot\frac{\Delta t_n}{||\mathbf{x}_{1,\ell}^2||}(\rho u_\xi u_\theta)_{A_{1,\ell}^2}^{n+\frac{1}{2}},\\
&(\rho E)_{1,\ell}^{n+1}=(\rho E)_{1,\ell}^{n}-3\cdot\frac{\Delta t_n}{||\mathbf{x}_{1,\ell}^2||}(u_\xi(\rho E+p))_{A_{1,\ell}^2}^{n+\frac{1}{2}},\quad \ell=1,\cdots,L,
\end{aligned}\tag{3.21}$$

where the middle-point value $\tilde{\mathbf{U}}_{A_{1,\ell}^2}^{n+\frac{1}{2}}$ can be obtained using the GRP solver in Subsection 2.1.

*Proof.* Proposition 3.2 shows that $u_\xi(0,\theta,t)\equiv 0$, $u_\theta(0,\theta,t)\equiv 0$.

For the evolution of mass, we apply the finite volume formulation for (2.3) over the control volume $C_\beta=I_\beta\times[t_n,t_{n+1}]$,

$$\int_{C_\beta}\xi^2\frac{\partial\rho}{\partial t}d\xi d\theta dt+\int_{C_\beta}\left(\frac{\partial(\xi^2\rho u_\xi)}{\partial\xi}+\frac{\partial(\xi^2\rho u_\theta)}{\partial\theta}\right)d\xi d\theta dt=0,\tag{3.22}$$

where $\beta=(1,\ell)$ and the factor $\xi$ plays an important role of the Jacobian in the transformation from the cylindrical coordinates to the spherical coordinates. Then a direct numerical integration formally tells

$$\int_{C_\beta}\xi^2\frac{\partial\rho}{\partial t}d\xi d\theta dt=\frac{(\varepsilon\Delta\xi)^3\Delta\theta}{3}(\rho^{n+1}-\rho_\beta^n)+\mathcal{O}((\Delta\xi)^5),\tag{3.23}$$

where $\rho_\beta^n$ is the average value of $\rho(\xi,\theta,t_n)$ over the cell $I_\beta$,

$$\rho_\beta^n=\frac{3}{(\varepsilon\Delta\xi)^3\Delta\theta}\int_{I_\beta}\rho\xi^2 d\xi d\theta.\tag{3.24}$$

We take the integration by parts for the second term in the left hand side of (3.22) to obtain

$$\begin{aligned}
\int_{C_\beta}\Big(\frac{\partial(\xi^2\rho u_\xi)}{\partial\xi}+\frac{\partial(\xi^2\rho u_\theta)}{\partial\theta}\Big)d\xi d\theta dt&=\int_{t_n}^{t_{n+1}}\int_{(\ell-1/2)\Delta\theta}^{(\ell+1/2)\Delta\theta}\xi^2\rho u_\xi(\cdot,t)|_0^{\varepsilon\Delta\xi}d\theta dt\\
&\quad+\int_{t_n}^{t_{n+1}}\int_0^{\varepsilon\Delta\xi}\xi^2\rho u_\theta|_{(\ell-1/2)\Delta\theta}^{(\ell+1/2)\Delta\theta}d\xi dt\\
&=(\varepsilon\Delta\xi)^2\int_{t_n}^{t_{n+1}}\int_{(\ell-1/2)\Delta\theta}^{(\ell+1/2)\Delta\theta}\rho u_\xi d\theta dt,
\end{aligned}\tag{3.25}$$

where the angular symmetric property $u_\theta(\xi,(\ell-1/2)\Delta\theta,t)=u_\theta(\xi,(\ell+1/2)\Delta\theta,t)$ is used.

As the mass, momentum and energy equations of (2.3) are considered separately, we obtain by incorporating (3.22) and (3.23),

$$\rho_\beta^{n+1}=\rho_\beta^n-\frac{3}{\varepsilon\Delta\xi\Delta\theta}\int_{t_n}^{t_{n+1}}\int_{(\ell-1/2)\Delta\theta}^{(\ell+1/2)\Delta\theta}\rho u_\xi(\varepsilon\Delta\xi,\theta,t)d\theta dt, \tag{3.26}$$

$$(\rho u_\xi)_\beta^{n+1}=(\rho u_\xi)_\beta^n-\frac{3}{\varepsilon\Delta\xi\Delta\theta}\int_{t_n}^{t_{n+1}}\int_{(\ell-1/2)\Delta\theta}^{(\ell+1/2)\Delta\theta}\rho u_\xi^2(\varepsilon\Delta\xi,\theta,t)d\theta dt, \tag{3.27}$$

$$(\rho u_\theta)_\beta^{n+1}=(\rho u_\theta)_\beta^n-\frac{3}{\varepsilon\Delta\xi\Delta\theta}\int_{t_n}^{t_{n+1}}\int_{(\ell-1/2)\Delta\theta}^{(\ell+1/2)\Delta\theta}\rho u_\xi u_\theta(\varepsilon\Delta\xi,\theta,t)d\theta dt, \tag{3.28}$$

$$(\rho E)_\beta^{n+1}=(\rho E)_\beta^n-\frac{3}{\varepsilon\Delta\xi\Delta\theta}\int_{t_n}^{t_{n+1}}\int_{(\ell-1/2)\Delta\theta}^{(\ell+1/2)\Delta\theta}u_\xi(\rho E+p)(\varepsilon\Delta\xi,\theta,t)d\theta dt. \tag{3.29}$$

Then the mid-point rule is used to evaluate the single time integrals and obtain (3.21) within second order accuracy. ☐

**Remark 3.1.** In literature, a reflection boundary condition for density and pressure is often used at the center directly, and the velocity is assumed to be zero. Thus, the source term does not take effect on the center cells. This leads to the inconsistency with governing Eq. (2.3). We will show the effect of these boundary conditions when they are applied to examples in Section 5.

At last we summarize the GRP scheme on the equal angular polar grid in the following.

**Step 1.** At $t_n=0$, initial Equal angular polar grid of the domain $\Omega$, the initial data $\tilde{\mathbf{U}}_{k,\ell}^n$ in (2.8), and the initial gradient $\boldsymbol{\oe}_{k,\ell}^n$ are given, where $k=1,\cdots,K$ and $\ell=1,\cdots,L$. Then the centroid value $\tilde{\mathbf{U}}_{A_{k,\ell}^j}^{n+\frac{1}{2}}$ for each cell $I_{k,\ell}$ is calculated with formula (2.13) by solving the local generalized Riemann problem (2.11), where $k=2,\cdots,K-1$ and $\ell=2,\cdots,L-1$.

**Step 2.** Evaluate the new cell averages $\tilde{\mathbf{U}}_{k,\ell}^{n+1}$ using (2.7), (2.9), and (2.10), where $k=2,\cdots,K-1$ and $\ell=2,\cdots,L-1$, and then obtain the new boundary cell averages $\tilde{\mathbf{U}}_{k,\ell}^{n+1}$ by applying the boundary conditions (3.1), (3.2), and (3.21).

**Step 3.** Update the gradient $\boldsymbol{\oe}_{k,\ell}^{n+1}$ with a monotonicity algorithm-slope limiter which is discussed in Section 2.2.

**Step 4.** Go to **Step 1** if $t_{n+1}<T$.

# 4 A Lagrangian GRP scheme with preservation of spherical symmetry in cylindrical coordinates

## 4.1 A Lagrangian formulation in cylindrical coordinates

In terms of Lagrangian coordinates, the compressible Euler equations are written as

$$\frac{d}{dt}\int_{\Omega(t)}\check{\mathbf{U}}dV+\int_{\Gamma(t)}\check{\mathbf{F}}ds=0, \tag{4.1}$$

with the geometry conservation law

$$\frac{d}{dt}\int_{\Omega(t)}dV=\int_{\Gamma(t)}\mathbf{u}\cdot\mathbf{n}ds, \tag{4.2}$$

where $\Omega(t)$ is a Lagrangian control volume, $\check{\mathbf{U}}=[\rho,\rho\mathbf{u},\rho E]$, $\check{\mathbf{F}}=[0,p\mathbf{n},p\mathbf{u}\cdot\mathbf{n}]$, $\Gamma(t)=\partial\Omega(t)$ and $\mathbf{n}$ is the outer unit normal of $\Gamma(t)$. In this paper, we aim to study the cylindrical symmetry compressible Euler system. Its specific form in the cylindrical coordinates takes

$$\frac{d}{dt}\int_{\Omega(t)}\check{\mathbf{U}}rdrdz+\int_{\Gamma(t)}\check{\mathbf{F}}rds=\int_{\Omega(t)}\tilde{\mathbf{\Psi}}drdz, \tag{4.3}$$

with the geometry conservation law

$$\frac{d}{dt}\int_{\Omega(t)}rdrdz=\int_{\Gamma(t)}\mathbf{u}\cdot\mathbf{n}rds, \tag{4.4}$$

where the source term $\tilde{\mathbf{\Psi}}=[0,0,p,0]$, and $u,v$ are velocity components in the $z$ and $r$ directions for $\mathbf{u}=(u,v)$ respectively, and $\mathbf{n}=(n_z,n_r)$ is the unit outward normal to the boundary $\Gamma(t)$ in the $z-r$ coordinates. The geometry conservation law (4.4) is compatible with the local kinematic equations

$$\frac{d\mathbf{X}}{dt}=\mathbf{u}, \quad \mathbf{X}(0)=\mathbf{x}, \tag{4.5}$$

where $\mathbf{X}=(z,r)$ are coordinates defining the control surface at time $t>0$ and $\mathbf{x}$ are the coordinates at time $t=0$. Thus, $\mathbf{X}=\mathbf{X}(\mathbf{x},t)$ are implicitly defined by the local kinematic equations, or called the trajectory equations.

## 4.2 The GRP scheme in Lagrangian formulation

In analogy with that in Eulerian coordinates, we also focus on an equal-angle-zone grid and construct a second-order scheme preserving the spherical symmetry and conservation properties in the cylindrical geometry. Thus in each cell $I_{k,\ell}$ we obtain the equivalent Euler system by performing the local coordinates transformation,

$$\frac{d}{dt}\int_{I_{k,\ell}}\grave{\mathbf{U}}rdrdz+\int_{\partial I_{k,\ell}}\grave{\mathbf{F}}rds=\int_{I_{k,\ell}}\hat{\mathbf{\Psi}}drdz, \tag{4.6}$$

where $\grave{\mathbf{U}}=[\rho,\rho u_\xi,\rho u_\theta,\rho E]$, $\grave{\mathbf{F}}=[0,pn_\xi,pn_\theta,pu_v]$, and $\hat{\mathbf{\Psi}}=[0,p\sin\phi,p\cos\phi,0]$, and $\mathbf{n}=(n_\xi,n_\theta)$ is the unit outward normal of the cell boundary $\partial I_{k,\ell}$ and $\phi$ is the angle between the radial direction passing through the corresponding point and the axial coordinate $z$. In the framework of cell-centered finite volume methods, all variables are stored at the cell center of $I_{k,\ell}$ in the form of cell averages. Thus the cell average $\bar{U}_{k,\ell}=(\bar{\rho},\overline{\rho u_\xi},\overline{\rho u_\theta},\overline{\rho E})_{k,\ell}$ is,

$$\bar{U}_{k,\ell}=\frac{1}{V_{k,\ell}}\int_{I_{k,\ell}} Urdrdz, \tag{4.7}$$

where $V_{k,\ell}=\int_{I_{k,\ell}} rdrdz$. The mass over the cell $I_{k,\ell}$ is denoted by $M_{k,\ell}=\bar{\rho}_{k,\ell}V_{k,\ell}$. Thus, the fully discretized scheme for (4.6) can be written as

$$\bar{U}^{n+1}_{k,\ell}V^{n+1}_{k,\ell}-\bar{U}^{n}_{k,\ell}V^{n}_{k,\ell}=\Delta t_n\Big(-\sum_{j=1}^{m}\hat{\mathbf{F}}(\grave{\mathbf{U}}^{n+\frac{1}{2}}_{A^j_{k,\ell}})\Delta\ell^{j,n+\frac{1}{2}}+\hat{\mathbf{S}}\Big), \tag{4.8}$$

where the numerical flux and the discretized source term are

$$\hat{\mathbf{F}}(\grave{\mathbf{U}}^{n+\frac{1}{2}}_{A^j_{k,\ell}})=\begin{pmatrix} 0, \\ n^j_\xi r_e^{j,n+\frac{1}{2}} p^{n+\frac{1}{2}}_{A^j_{k,\ell}} \\ n^j_\theta r_e^{j,n+\frac{1}{2}} p^{n+\frac{1}{2}}_{A^j_{k,\ell}} \\ u_v^{j,n+\frac{1}{2}} r_e^{j,n+\frac{1}{2}} p^{n+\frac{1}{2}}_{A^j_{k,\ell}} \end{pmatrix}, \quad \hat{\mathbf{S}}=\begin{pmatrix} 0 \\ (\tilde{p}_c)^{n+\frac{1}{2}}_{k,\ell}\sin(\phi_c)^{n+\frac{1}{2}}_k S^{n+\frac{1}{2}}_{k,\ell} \\ (p_c)^{n+\frac{1}{2}}_{k,\ell}\cos(\phi_c)^{n+\frac{1}{2}}_k S^{n+\frac{1}{2}}_{k,\ell} \\ 0 \end{pmatrix}, \tag{4.9}$$

and $(p_c)_{k,\ell}$, $(\tilde{p}_c)_{k,\ell}$ in the source term denote

$$(p_c)_{k,\ell}=\frac{1}{2}(p^1+p^3), \quad (\tilde{p}_c)_{k,\ell}=\frac{1}{2}(p^2+p^4). \tag{4.10}$$

Here $p^1$, $p^2$, $p^3$ and $p^4$ are the values of the pressure at edges 1, 2, 3 and 4 of cell $I_{k,\ell}$ in Fig. 1, $(n^j_\xi,n^j_\theta)$ and $r^j_e$ are the unit normal direction and the $r$ coordinate of the middle point of edge $j$, respectively; the velocity $u_v^{j,n+\frac{1}{2}}$ is equal to $(u_\xi^{j,n+\frac{1}{2}},u_\theta^{j,n+\frac{1}{2}})\cdot(n^j_\xi,n^j_\theta)$. The local GRP solver in the Lagrangian type for $\grave{\mathbf{U}}^{n+\frac{1}{2}}_{A^j_{k,\ell}}$ can be obtained in the same way in [23].

The trajectory equations (4.5) can also be discretized as follows

$$\frac{\mathbf{X}^{n+1}_\alpha-\mathbf{X}^n_\alpha}{\Delta t_n}=\mathbf{u}^{n+\frac{1}{2}}_\alpha, \tag{4.11}$$

where $\alpha=(k+1/2,\ell+1/2)$ is the one of vertexes on the boundary of the control volume $I_{k,\ell}$.

In the following we will verify that the GRP scheme (4.8) can keep the spherical symmetry property on the equal-angle-zoned initial grid in Fig. 1.

**Theorem 4.1.** *If the initial data $\bar{U}^0_{k,\ell}$ and the gradient $\sigma^0_{k,\ell}$ have one dimensional spherical symmetry on the equal-angle zoned initial grid, then the computational solution $\bar{U}^{n+1}_{k,\ell}$ of the GRP scheme* (4.8) *and the gradient $\sigma^{n+1}_{k,\ell}$ will keep the one dimensional spherical property with the time going. That is, the solution and the gradient depend only on the radial distance $\xi$.*

*Proof.* In fact, we only need to prove $\bar{U}^{n+1}_{k,\ell}$ and $\sigma^{n+1}_{k,\ell}$ keep the spherical symmetry by assuming $\bar{U}^n_{k,\ell}$ and $\sigma^n_{k,\ell}$ are in spherical symmetry. "Spherical symmetry" means that the grid is a polar grid with equal angles (see Fig. 1) and the cell averages of the conserved variables and their gradient are symmetry on the grid, namely these variables in the cells with the same $k$ are identical. For simplicity, we omit the subscript "$\ell$" for the variables,

$$\bar{U}^n_{k,\ell}=\bar{U}_k, \quad \sigma^n_{k,\ell}=\sigma_k, \quad k=1,\cdots,K, \quad \ell=1,\cdots,L, \tag{4.12}$$

where $\bar{U}_k=(\bar{\rho}_k,\overline{\rho u_\xi}_k,\overline{\rho u_\theta}_k,\overline{\rho E}_k)^T=(\bar{\rho}_k,\overline{\rho u_\xi}_k,0,\overline{\rho E}_k)^T$ and $\sigma_k$ is the gradient of $U_k$. The proof is similar to the way in Cheng and Shu's paper [16], including two steps. In the first step, we need to verify the grid at $(n+1)-$th time step is symmetrical. In the second step, we should prove that the conserved variables $\bar{U}^{n+1}_{k,\ell}$ and the gradient $\sigma^{n+1}_{k,\ell}$ keep the spherical symmetry.

First we define some variables relating to the grid geometry. For simplicity, we omit the subscript "$(k,\ell)$" for the quantities corresponding to the cell edge if no confusion is caused. Denote $\Delta\phi$ as the angle between any two neighboring $\ell$ lines which is a constant for the equi-angular polar grid. Since the grid is symmetrical, the middle point of the edge $\xi^j_e$ and the length of the edge $\Delta\ell^j$, for $j=1,4$, are independent of the $\ell$ index. Thus we obtain

$$\xi^1_e=\xi^3_e=\xi_k, \quad \xi^2_e=\xi_{k+1/2}, \quad \xi^4_e=\xi_{k-1/2}, \tag{4.13}$$

$$\Delta\ell^1=\Delta\ell^3=\Delta\ell_k, \quad \Delta\ell^2=\Delta\ell_{k+1/2}, \quad \Delta\ell^4=\Delta\ell_{k-1/2}. \tag{4.14}$$

Moreover, the outward normal direction $\mathbf{n}=(n_\xi,n_\theta)$ of the four edges of the cell in the local $\xi-\theta$ coordinates are the following,

$$(n_\xi,n_\theta)^1=\left(-\sin\left(\frac{1}{2}\Delta\phi\right),-\cos\left(\frac{1}{2}\Delta\phi\right)\right), \quad (n_\xi,n_\theta)^2=(1,0), \tag{4.15}$$

$$(n_\xi,n_\theta)^3=\left(-\sin\left(\frac{1}{2}\Delta\phi\right),\cos\left(\frac{1}{2}\Delta\phi\right)\right), \quad (n_\xi,n_\theta)^4=(-1,0). \tag{4.16}$$

Next we will prove the symmetry of the grid at the $(n+1)-$th step.

For this purpose, we want to find out the velocity on each cell edge and need to determine $U^{j\pm}_\nu=(\rho^{j\pm},(\rho u_\nu)^{j\pm},(\rho E)^{j\pm})$ and $(\rho u_\tau)^{j\pm}$, for $j=1,\cdots,4$, where $(\rho u_\tau)^{j\pm}$ is the tangential momentum at the two sides of edge $j$, $(\rho^j,(\rho u_\nu)^j,(\rho E)^j)$ denote density, normal momentum and total energy at the edge which are obtained from $U^{j\pm}_\nu$ through the Riemann solver and the GRP solver. The pressure, normal velocity and tangent velocity at edge $j$ are defined as $p^j$, $u^j_\nu$, $u^j_\tau$, respectively, $u^j_\tau=((\rho u_\tau)^{j-}/\rho^{j-}+(\rho u_\tau)^{j+}/\rho^{j+})/2$.

In order to use the local one dimensional GRP solver and Riemann solver, we obtain the $U_\nu^{j\pm}$ and $(\rho u_\tau)^{j\pm}$, for $j=2,4$,

$$U_\nu^{2-}=(\rho_{k+1/2}^{2-},(\rho u_\xi)_{k+1/2}^{2-},(\rho E)_{k+1/2}^{2-}),\quad (\rho u_\tau)^{2-}=(\rho u_\theta)_{k+1/2}^{2-}=0, \tag{4.17}$$

$$U_\nu^{2+}=(\rho_{k+1/2}^{2+},(\rho u_\xi)_{k+1/2}^{2+},(\rho E)_{k+1/2}^{2+}),\quad (\rho u_\tau)^{2+}=(\rho u_\theta)_{k+1/2}^{2+}=0, \tag{4.18}$$

$$U_\nu^{4-}=(\rho_{k-1/2}^{4-},(\rho u_\xi)_{k-1/2}^{4-},(\rho E)_{k-1/2}^{4-}),\quad (\rho u_\tau)^{4-}=(\rho u_\theta)_{k-1/2}^{4-}=0, \tag{4.19}$$

$$U_\nu^{4+}=(\rho_{k-1/2}^{4+},(\rho u_\xi)_{k-1/2}^{4+},(\rho E)_{k-1/2}^{4+}),\quad (\rho u_\tau)^{4+}=(\rho u_\theta)_{k-1/2}^{4+}=0, \tag{4.20}$$

where the notations are

$$U_{k+1/2}^{2-}=\bar{U}_k+\sigma_k\cdot\mathbf{n}^2||\mathbf{x}_e^2-\mathbf{x}_{k,\ell}||,\quad U_{k+1/2}^{2+}=\bar{U}_{k+1}-\sigma_{k+1}\cdot\mathbf{n}^2\|\mathbf{x}_{k+1,\ell}-\mathbf{x}_e^2\|, \tag{4.21}$$

$$U_{k-1/2}^{4-}=\bar{U}_{k-1}-\sigma_{k-1}\cdot\mathbf{n}^4||\mathbf{x}_e^4-\mathbf{x}_{k-1,\ell}\|,\quad U_{k-1/2}^{4+}=\bar{U}_k+\sigma_k\cdot\mathbf{n}^4\|\mathbf{x}_{k,\ell}-\mathbf{x}_e^4\|. \tag{4.22}$$

Similarly, we can obtain $U_\nu^{j\pm}$ and $(\rho u_\tau)^{j\pm}$, for $j=1,3$, by projecting the momentum of the neighboring cells in their local $\xi$, $\theta$ directions to those of cell $I_{k,\ell}$,

$$U_\nu^{1-}=\left(\rho_k^{1-},-(\rho u_\xi)_k^{1-}\sin\left(\frac{\Delta\phi}{2}\right),(\rho E)_k^{1-}\right),\quad (\rho u_\tau)^{1-}=(\rho u_\xi)_k^{1-}\cos\left(\Delta\frac{\phi}{2}\right), \tag{4.23}$$

$$U_\nu^{1+}=\left(\rho_k^{1+},(\rho u_\xi)_k^{1+}\sin\left(\frac{\Delta\phi}{2}\right),(\rho E)_k^{1+}\right),\quad (\rho u_\tau)^{1+}=(\rho u_\xi)_k^{1+}\cos\left(\Delta\frac{\phi}{2}\right), \tag{4.24}$$

$$U_\nu^{3-}=\left(\rho_k^{3-},-(\rho u_\xi)_k^{3-}\sin\left(\frac{\Delta\phi}{2}\right),(\rho E)_k^{3-}\right),\quad (\rho u_\tau)^{3-}=(\rho u_\xi)_k^{3-}\cos\left(\Delta\frac{\phi}{2}\right), \tag{4.25}$$

$$U_\nu^{3+}=\left(\rho_k^{3+},(\rho u_\xi)_k^{3+}\sin\left(\frac{\Delta\phi}{2}\right),(\rho E)_k^{3+}\right),\quad (\rho u_\tau)^{3+}=(\rho u_\xi)_k^{3+}\cos\left(\Delta\frac{\phi}{2}\right), \tag{4.26}$$

where we define

$$U_k^{1-}=\bar{U}_k+\sigma_k\cdot\mathbf{n}^1||\mathbf{x}_e^1-\mathbf{x}_{k,\ell}\|,\quad U_k^{1+}=\bar{U}_k-\sigma_k\cdot\mathbf{n}^1\|\mathbf{x}_e^1-\mathbf{x}_{k,\ell-1}||, \tag{4.27}$$

$$U_k^{3-}=\bar{U}_k-\sigma_k\cdot\mathbf{n}^3\|\mathbf{x}_e^3-\mathbf{x}_{k,\ell+1}||,\quad U_k^{3+}=\bar{U}_k+\sigma_k\cdot\mathbf{n}^3||\mathbf{x}_e^3-\mathbf{x}_{k,\ell}\|. \tag{4.28}$$

By the Riemann solver and GRP solver, we obtain

$$u_\nu^1=u_\nu^3=0,\quad u_\nu^2=(u_\nu)_{k+1/2}^{n+1/2},\quad u_\nu^4=-(u_\nu)_{k-1/2}^{n+1/2}, \tag{4.29}$$

$$p^1=p^3=p_k,\quad p^2=p_{k+1/2}^{n+1/2},\quad p^4=p_{k-1/2}^{n+1/2}, \tag{4.30}$$

which are independent of the "$\ell$" index since $U_\nu^{2\pm}$ and $U_\nu^{4\pm}$ are independent of the "$\ell$" index. The tangential velocities at each edge are obtained as follows,

$$u_\tau^1=\cos\left(\frac{\Delta\phi}{2}\right)(u_\xi)_k^1,\quad u_\tau^3=\cos\left(\frac{\Delta\phi}{2}\right)(u_\xi)_k^3,\quad u_\tau^2=0,\quad u_\tau^4=0, \tag{4.31}$$

where $(u_\xi)_k^1=(u_\xi)_k^3$ indicates $u_\tau^1=u_\tau^3$. By now we can conclude that all the values of the velocity and pressure are independent of the "$\ell$" index.

Since the grid is equi-angular, we can easily get the velocity at the vertex $(k+1/2,\ell+1/2)$,

$$\mathbf{u}^{n+1/2}_{k+1/2,\ell+1/2}=\frac{(u_v)^{n+1/2}_{k+1/2}}{\cos(\frac{\Delta\phi}{2})}\mathbf{n}_{k+1/2,\ell+1/2}, \tag{4.32}$$

where $\mathbf{n}_{k+1/2,\ell+1/2}$ is a unit direction from the vertex $(0,0)$ to $(k+1/2,\ell+1/2)$. The above identity (4.32) indicates the velocity at the vertices with the same $k$ index are identical and their directions are taken along their radial directions. Thus we have completed the proof of the symmetry of the grid at the $(n+1)-$th step by the discretized trajectory equations (4.11).

Finally we will prove that the symmetry can also be preserved for the evolved conserved variables $\bar{U}^{n+1}_{k,\ell}$. With the symmetry property of grid at $(n+1)$-th step, the area and volume of cell $I_{k,\ell}$ at the $(n+1)$-th step can be read simply as follows,

$$S^{n+1}_{k,\ell}=S^{n+1}_{k}, \quad V^{n+1}_{k,\ell}=(r_c)^{n+1}_{k,\ell}S^{n+1}_{k}=(\xi_c)^{n+1}_{k}\sin(\phi_c)_\ell S^{n+1}_{k}, \tag{4.33}$$

where $r_c$ and $\xi_c$ are the values of $r$ and $\xi$ at the cell center, respectively. We have omitted the subscript "$\ell$" of the variables since we have verified that the grid at the $(n+1)$-th step is symmetrical. We also have omitted the subscript "$k$" and superscript "$n+1$" of $\phi_c$ since it is independent of the $k$ and $n$ indices. Therefore we can rewrite the term at the left hand of (4.8) as follows,

$$\bar{U}^{n+1}_{k,\ell}V^{n+1}_{k,\ell}-\bar{U}^{n}_{k,\ell}V^{n}_{k,\ell}=\sin(\phi_c)_\ell[\bar{U}^{n+1}_{k,\ell}(\xi_c)^{n+1}_{k}S^{n+1}_{k}-\bar{U}_k(\xi_c)_kS_k]. \tag{4.34}$$

The flux term in (4.8) can be expressed as follows

$$\sum_{j=1}^{m}\hat{\mathbf{F}}(U^{n+\frac{1}{2}}_{A^j_{k,\ell}})\Delta\ell^{j,n+\frac{1}{2}}=\left(\begin{array}{c} 0 \\ -p^1\sin(\frac{\Delta\phi}{2})\Delta\ell^1(r^1_e+r^3_e)+p^2r^2_e\Delta\ell^2-p^4r^4_e\Delta\ell^4 \\ p^1\Delta\ell^1(r^3_e-r^1_e)\cos(\frac{\Delta\phi}{2}) \\ p^2u^2_vr^2_e\Delta\ell^2+p^4u^4_vr^4_e\Delta\ell^4 \end{array}\right). \tag{4.35}$$

Using (4.13), (4.14), (4.29), (4.30) and following expressions

$$r^1_e=\xi_k\sin\Big((\phi_c)_\ell-\frac{\Delta\phi}{2}\Big), \qquad r^2_e=\xi_{k+\frac{1}{2}}\sin(\phi_c)_\ell, \tag{4.36}$$

$$r^3_e=\xi_k\sin\Big((\phi_c)_\ell+\frac{\Delta\phi}{2}\Big), \qquad r^4_e=\xi_{k-\frac{1}{2}}\sin(\phi_c)_\ell, \tag{4.37}$$

we have

$$
\begin{aligned}
&\sum_{j=1}^{m}\hat{\mathbf{F}}(U^{n+\frac{1}{2}}_{A^j_{k,\ell}})\Delta\ell^{j,n+\frac{1}{2}}\\
=&\begin{pmatrix}
0\\
\sin(\phi_c)_\ell(-p_k^{n+\frac{1}{2}}\xi_k^{n+\frac{1}{2}}\Delta\ell_k^{n+\frac{1}{2}}\sin(\Delta\phi)+p_{k+\frac{1}{2}}^{n+\frac{1}{2}}\xi_{k+\frac{1}{2}}^{n+\frac{1}{2}}\Delta\ell_{k+\frac{1}{2}}^{n+\frac{1}{2}}-p_{k-\frac{1}{2}}^{n+\frac{1}{2}}\xi_{k-\frac{1}{2}}^{n+\frac{1}{2}}\Delta\ell_{k-\frac{1}{2}}^{n+\frac{1}{2}})\\
p_k^{n+\frac{1}{2}}S_k^{n+\frac{1}{2}}\cos(\phi_c)_\ell\\
\sin(\phi_c)_\ell(p_{k+\frac{1}{2}}^{n+\frac{1}{2}}(u_\nu)_{k+\frac{1}{2}}^{n+\frac{1}{2}}\xi_{k+\frac{1}{2}}^{n+\frac{1}{2}}\Delta\ell_{k+\frac{1}{2}}^{n+\frac{1}{2}}-p_{k-\frac{1}{2}}^{n+\frac{1}{2}}(u_\nu)_{k-\frac{1}{2}}^{n+\frac{1}{2}}\xi_{k-\frac{1}{2}}^{n+\frac{1}{2}}\Delta\ell_{k-\frac{1}{2}}^{n+\frac{1}{2}})
\end{pmatrix},
\end{aligned}
\tag{4.38}
$$

where $\xi^{n+\frac{1}{2}}=(\xi^{n+1}+\xi^n)/2$, $\Delta\ell^{n+\frac{1}{2}}=(\Delta\ell^n+\Delta\ell^{n+1})/2$, and $p^{n+\frac{1}{2}}$, $(u_\nu)^{n+\frac{1}{2}}$ are obtained by the local one dimensional GRP solver and Riemann solver. Using the equalities in (4.10), the source term in (4.8) reads as follows

$$
\hat{\mathbf{S}}=\begin{pmatrix}
0\\
(\tilde{p}_c)_{k,\ell}^{n+\frac{1}{2}}\sin(\phi_c)_k^{n+\frac{1}{2}}S_{k,\ell}^{n+\frac{1}{2}}\\
(p_c)_{k,\ell}^{n+\frac{1}{2}}\cos(\phi_c)_k^{n+\frac{1}{2}}S_{k,\ell}^{n+\frac{1}{2}}\\
0
\end{pmatrix}=\begin{pmatrix}
0\\
\tilde{p}_k^{n+\frac{1}{2}}S_k^{n+\frac{1}{2}}\sin(\phi_c)_\ell\\
p_k^{n+\frac{1}{2}}S_k^{n+\frac{1}{2}}\cos(\phi_c)_\ell\\
0
\end{pmatrix}. \tag{4.39}
$$

Thus the Lagrangian GRP scheme (4.8) can be written

$$
\begin{aligned}
\bar{U}_{k,\ell}^{n+1}=&\frac{(\xi_c)_k^nS_k^n}{(\xi_c)_k^{n+1}S_k^{n+1}}\bar{U}_{k,\ell}^n+\frac{\Delta t_n}{(\xi_c)_k^{n+1}S_k^{n+1}}\\
&\begin{pmatrix}
0\\
p_k^{n+\frac{1}{2}}\xi_k^{n+\frac{1}{2}}\Delta\ell_k^{n+\frac{1}{2}}\sin(\Delta\phi)-p_{k+\frac{1}{2}}^{n+\frac{1}{2}}\xi_{k+\frac{1}{2}}^{n+\frac{1}{2}}\Delta\ell_{k+\frac{1}{2}}^{n+\frac{1}{2}}+p_{k-\frac{1}{2}}^{n+\frac{1}{2}}\xi_{k-\frac{1}{2}}^{n+\frac{1}{2}}\Delta\ell_{k-\frac{1}{2}}^{n+\frac{1}{2}}+\tilde{p}_k^{n+\frac{1}{2}}S_k^{n+\frac{1}{2}}\\
0\\
-p_{k+\frac{1}{2}}^{n+\frac{1}{2}}(u_\nu)_{k+\frac{1}{2}}^{n+\frac{1}{2}}\xi_{k+\frac{1}{2}}^{n+\frac{1}{2}}\Delta\ell_{k+\frac{1}{2}}^{n+\frac{1}{2}}+p_{k-\frac{1}{2}}^{n+\frac{1}{2}}(u_\nu)_{k-\frac{1}{2}}^{n+\frac{1}{2}}\xi_{k-\frac{1}{2}}^{n+\frac{1}{2}}\Delta\ell_{k-\frac{1}{2}}^{n+\frac{1}{2}}
\end{pmatrix}.
\end{aligned}
\tag{4.40}
$$

By the initial condition (4.12), we can conclude that $\bar{U}_{k,\ell}^{n+1}$ only depend on the $k$ index and are independent of the index $\ell$. Then we can update the gradient $\sigma_{k,l}^{n+1}=(U_\xi,U_\theta)_{k,\ell}^{n+1}$ by the limiters proposed in Subsection 2.2. Thus we have completed the proof of symmetry preservation property of the GRP scheme (4.8). ☐

## 4.3 The boundary condition at the center

In the Lagrangian formulation for the Euler equation, we can obtain the following boundary condition at the center.

**Proposition 4.1.** At the center $(z,r)=(0,0)$ (or $(\xi,\theta)=(0,\theta)$), the velocity must vanish, i.e. $u_\xi(0,\theta,t)=0$, $u_\theta(0,\theta,t)=0$, and there exist a control volume $\Omega_\varepsilon(t)$ with a radius $\varepsilon\to 0$, such that the mass, energy, and momentum satisfy

$$\frac{d}{dt}\int_{\Omega_\varepsilon(t)}\rho r dr dz=0, \tag{4.41}$$

$$\frac{d}{dt}\int_{\Omega_\varepsilon(t)}\rho E r dr dz+\int_{\partial\Omega_\varepsilon(t)}p(u_\xi,u_\theta)\cdot(n_\xi,n_\theta)r ds=0, \tag{4.42}$$

$$\frac{d}{dt}\int_{\Omega_\varepsilon(t)}\rho(u_\xi,u_\theta)r dr dz+\int_{\partial\Omega_\varepsilon(t)}p(n_\xi,n_\theta)r ds=\int_{\Omega_\varepsilon(t)}p(\sin\phi,\cos\phi)dr dz, \tag{4.43}$$

with the geometry conservation law

$$\frac{d}{dt}\int_{\Omega_\varepsilon(t)}r dr dz=\int_{\partial\Omega_\varepsilon(t)}(u_\xi,u_\theta)\cdot(n_\xi,n_\theta)r ds. \tag{4.44}$$

Thus we can have the following numerical boundary condition at the center approximately.

**Proposition 4.2.** $I_0(t)$ is a cell with a radius $\varepsilon>0$ at the center. Then the numerical boundary condition at the center can be expressed as follows approximately

$$(\rho)_c^{n+1}V_0^{n+1}=(\rho)_c^0V_0^0, \tag{4.45}$$

$$(\rho\mathbf{u})_c^{n+1}=(\rho\mathbf{u})_c^n-\Delta t_n\sum_{j=1}^m p_{A_0^j}^{n+\frac{1}{2}}\mathbf{n}r_e^{j,n+\frac{1}{2}}\Delta\ell^{j,n+\frac{1}{2}}+\Delta t_n p_c^{n+\frac{1}{2}}(\sin\phi_c,\cos\phi_c)S_0^{n+\frac{1}{2}}, \tag{4.46}$$

$$(\rho E)_c^{n+1}V_0^{n+1}=(\rho E)_c^{n+1}V_0^{n+1}-\Delta t_n\sum_{j=1}^m p_{A_0^j}^{n+\frac{1}{2}}\mathbf{u}_{A_0^j}^{n+\frac{1}{2}}\cdot\mathbf{n}r_e^{j,n+\frac{1}{2}}\Delta\ell^{j,n+\frac{1}{2}},\quad m=3, \tag{4.47}$$

with the geometry conservation law

$$V_0^{n+1}=V_0^n+\Delta t_n\sum_{j=1}^m\mathbf{u}_{A_0^j}^{n+\frac{1}{2}}\cdot\mathbf{n}r_e^{j,n+\frac{1}{2}}\Delta\ell^{j,n+\frac{1}{2}},\quad m=3, \tag{4.48}$$

where $p_{A_0^j}^{n+\frac{1}{2}}$ and $\mathbf{u}_{A_0^j}^{n+\frac{1}{2}}$ are obtained by the local one dimensional GRP solver and Riemann solver, and the subscript $c$ denotes the average value over the cell $I_0(t)$ and $V_0=\int_{I_0(t)}r dr dz$ and $S_0=\int_{I_0(t)}dr dz$.

## 5 Numerical experiments

In this section we present several typical examples. The purpose is to illustrate the performance of the current scheme. In the following numerical examples, $\gamma>1$ is the adiabatic index and the Courant number $\mu_{CFL}$ is defined as

$$\mu_{CFL}=\Delta t_n \max_{k,\ell} \frac{||w^n_{k,\ell}||+c^n_{k,\ell}}{\Delta \ell_{k,\ell}}, \tag{5.1}$$

where $\Delta\ell_{k,\ell}$ is the shortest edge length of the cell $I_{k,\ell}$, and $w^n_{k,\ell}=(u^n_{k,\ell},v^n_{k,\ell})$, $c^n_{k,\ell}$ are the velocity and the sound speed with this cell, respectively. Here $||w^n_{k,\ell}||=\sqrt{(u^n_{k,\ell})^2+(v^n_{k,\ell})^2}$.

We take $\mu_{CFL}=0.4$ for all the examples. For the verification of the present scheme, we compare the GRP results with the corresponding exact solutions.

## 5.1 Accuracy test

We test the accuracy of the Lagrangian GRP scheme on a free expansion problem given in [33]. The gas is initially at rest with $\gamma=5/3$, having the following distribution

$$(\rho,u_\xi,u_\theta,p)=(1,0,0,1-(z^2+r^2)), \qquad (\theta,\xi)\in[0,\pi/2]\times[0,1]. \tag{5.2}$$

The analytical solution of this problem reads as follows

$$(\rho,u_\xi,u_\theta,p)(z,r,t)=\left(\frac{1}{R^3},\frac{2t}{1+2t^2}\sqrt{z^2+r^2},0,\frac{1}{R^5}\left(1-\frac{z^2+r^2}{R^2}\right)\right), \quad R(t)=\sqrt{1+2t^2}, \tag{5.3}$$

where $R$ is the radius of the free outer boundary.

The $L_\infty$ and $L_1$ numerical errors are listed in Table 1, where free boundary condition is applied on the outer boundary. Table 1 illustrates that the Lagrangian GRP scheme achieves the expected second order accuracy for all the variables.

Table 1: The $L_\infty$ and $L_1$ numerical errors at $T=1$ that are computed by the Lagrangian GRP scheme for the free expansion problem using $K\times L$ initially equi-angular polar grid cells.

| $K=L$ | Norm | Density | order | Velocity | order | Pressure | order |
|---|---|---|---|---|---|---|---|
| 20 | $L_\infty$ | 1.27(-4) | – | 4.59(-4) | – | 7.54(-4) | – |
| | $L_1$ | 2.65(-4) | – | 8.16(-4) | – | 9.52(-4) | – |
| 40 | $L_\infty$ | 3.36(-5) | 1.92 | 1.24(-4) | 1.89 | 1.98(-4) | 1.93 |
| | $L_1$ | 6.91(-5) | 1.94 | 2.17(-4) | 1.91 | 2.46(-4) | 1.95 |
| 80 | $L_\infty$ | 8.52(-6) | 1.98 | 3.19(-5) | 1.96 | 5.23(-5) | 1.92 |
| | $L_1$ | 1.76(-5) | 1.97 | 5.70(-5) | 1.93 | 6.32(-5) | 1.96 |
| 160 | $L_\infty$ | 2.24(-6) | 1.93 | 8.43(-6) | 1.92 | 1.35(-5) | 1.95 |
| | $L_1$ | 4.75(-5) | 1.89 | 1.51(-5) | 1.91 | 1.57(-5) | 2.01 |

## 5.2 Noh problem

The second example is the spherically converging flow of a cold (zero-pressure) perfect gas with $\Gamma=5/3$, having the uniform initial conditions

$$(\rho,u_\xi,u_\theta,p)=(1,-1,0,0),\quad (\theta,\xi)\in[0,\pi/2]\times[0,1], \tag{5.4}$$

which has been proposed by Noh [31] as a testing case having an exact (self-similar) solution. See also [27,32] for some recent simulations. The solution consists of an expanding spherical shock (starting from the center at $t=0$). The fluid behind the shock is quiescent with uniform pressure $p$ and density $\rho$. We set initial pressure to be $10^{-6}$ instead of zeros pressure. We take the boundary value over the cells $I_{K,\ell}$, $\ell=1,\cdots,L$,

$$(\rho,u_\xi,u_\theta,p)^{n+1}(z,r)=\left(\left(1+\frac{t_{n+1}}{\sqrt{r^2+z^2}}\right)^2,-1,0,10^{-6}\right),\quad (z,r)\in I_{K,\ell}, \tag{5.5}$$

which is the exact solution at $t=t_{n+1}$. We have shown the results of the Noh problem in Figs. 3 and 4. The results match the exact solution except for the discrepancies occurring primarily for the density distribution near the center. The book [7] explained that this error is due to the "startup" of the captured shock near the center, where the numerical dissipation generates an entropy higher than the exact value. These discrepancies can weakened by using the exact value of solution as the boundary data at the center [4]. We can see that the current scheme produces a good result in Fig. 3 by comparing with those in [27, 32]. The shock location and the shock magnitude obtained by the GRP scheme are close to the analytical solution. Moreover, the density at the center is less dissipative than other results [16]. In contrast, there are numerical oscillations near the center if the reflection boundary condition is applied, which illustrates that the reflection boundary condition is not applicable for this numerical case. Fig. 4 displays the two-dimensional results of the density, velocity and pressure which keep the symmetry.

Furthermore, from Fig. 3 we can see that the density distribution result of two-dimensional case matches better to the exact solution than that in one-dimensional case. Because the cells in the center in two-dimensional case are smaller than that in one-dimensional case, the dissipation in the center is weaker than that in one-dimensional case. In addition, we show the Lagrangian results in Fig. 5. It shows the final grid at $T=0.6$ with $300\times 20$ cells and the density as a function of radius at $T=0.6$. From the left part of Fig. 5, we observe that the two-dimensional grid is symmetric at $T=0.6$. From the right part of Fig. 5, we find that there is no spurious oscillation near the shock region. The shock location and the shock magnitude are close to the analytical solution.

## 5.3 The Sedov-Taylor blast wave problem

In the third test, we choose the Sedov-Taylor blast wave problem to simulate strong shock propagation. There exist numerical difficulties in the low density and high temperature near the center. Sedov [33] gave the analytical solution under the assumption that the

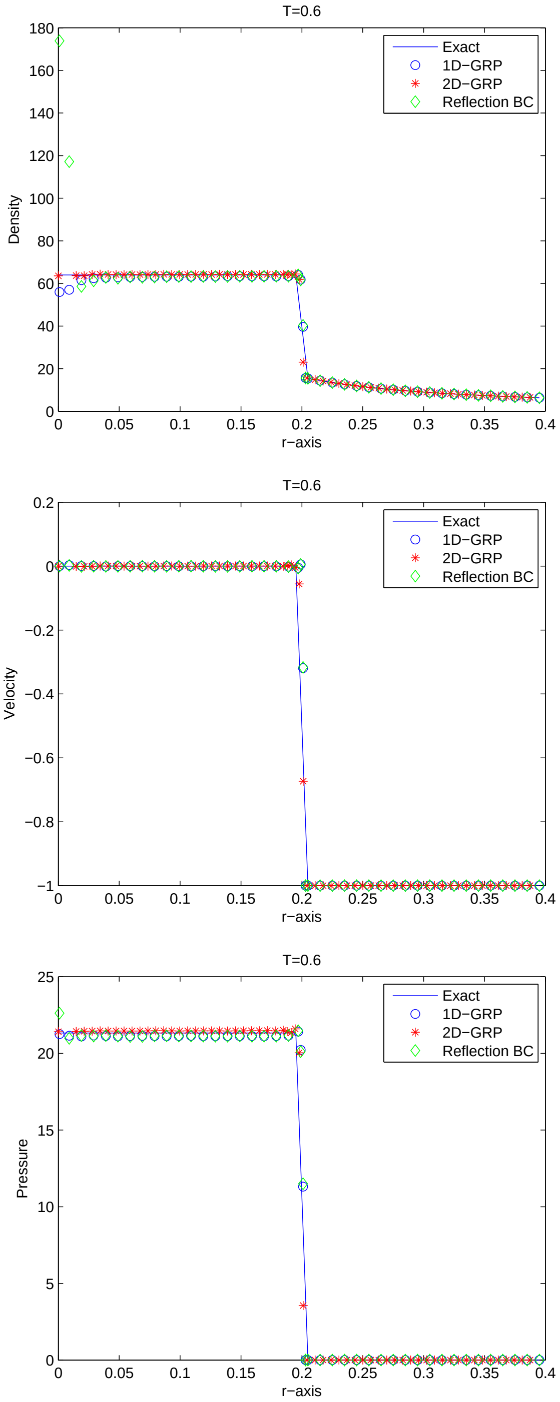

Figure 3: Numerical results for Noh problem by the Eulerian GRP scheme: $300\times 20$ grids are used for the two-dimensional case.

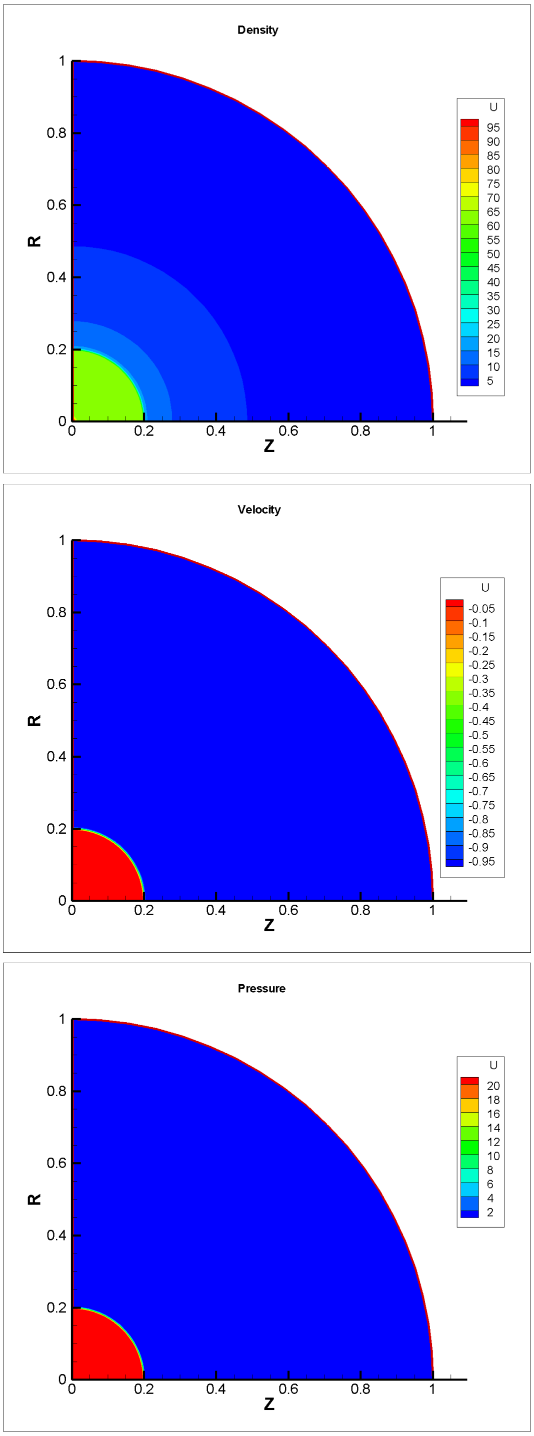

Figure 4: The contour of $\rho$, $u$, $p$ at $T=0.6$ for Noh problem by the Eulerian GRP scheme: $300\times 20$ grids are used.

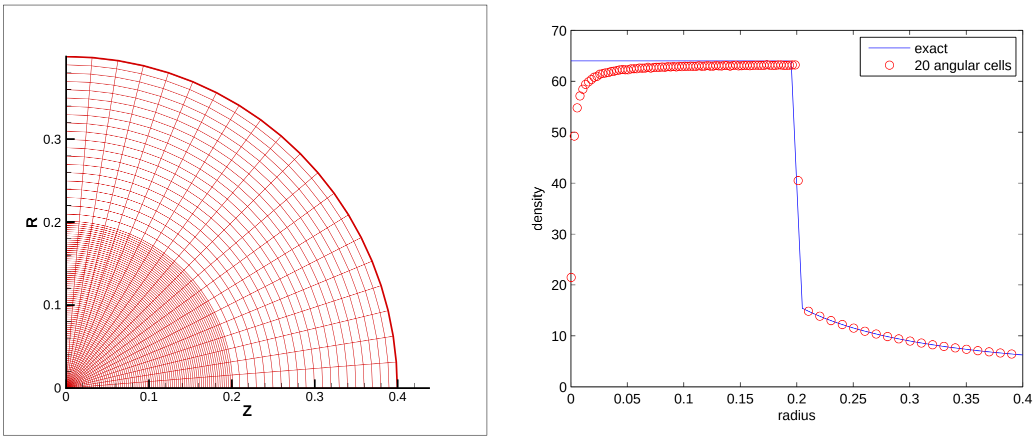

Figure 5: The result of the Noh problem at $T=0.6$ by the Lagrangian GRP scheme. Left: final grid with $300\times 20$ cells; Right: exact solution and computational solution for the density.

atmospherical pressure relative to the pressure inside the explosion is negligible. The gas is initially at rest with $\gamma=1.4$, having the following initial conditions,

$$(\rho,u_\xi,u_\theta,p)(r,z)=\begin{cases}(1,0,0,0.3406808), & (r,z)\in I_{1,\ell},\quad \ell=1,\cdots,L,\\ (1,0,0,10^{-6}), & \text{else}.\end{cases} \tag{5.6}$$

The initial computational domain is a $1/4-$circle region defined in the polar coordinates by $[0,\pi/2]\times[0,1.2]$ consisting of $300\times 20$ equi-angular polar grids. The analytical solution is a shock at $r=1$ at $T=1$. Fig. 6 demonstrates that the numerical results from GRP scheme are in quite satisfactory agreement with the analytical solution without any spurious oscillations. In addition, the reflection boundary condition at the center supports this numerical test. We also find that the numerical results are symmetrical from Fig. 7.

Fig. 8 shows the Lagrangian results of the Sedov problem. We find that it preserves symmetry for the two-dimensional grid at $T=1$. In addition, we observe that the position of shock and peak density are quite satisfactory in comparison with the analytical solution without any spurious oscillations, which demonstrates the good performance of the Lagrangian GRP scheme in symmetrical, non-oscillatory and accuracy properties.

## 5.4 The numerical simulation of spherical explosion in air

Brode [11] analyzed the spherical explosion model, which was investigated experimentally in [10] and simulated in [26]. The gas is initially at rest with $\gamma=1.4$, having the following initial conditions,

$$(\rho,u_\xi,u_\theta,p)(r,z)=\begin{cases}(21.7333,0,0,15.514), & \sqrt{r^2+z^2}\le 5,\\ (2,0,0,1), & 5<\sqrt{r^2+z^2}\le 50.\end{cases} \tag{5.7}$$

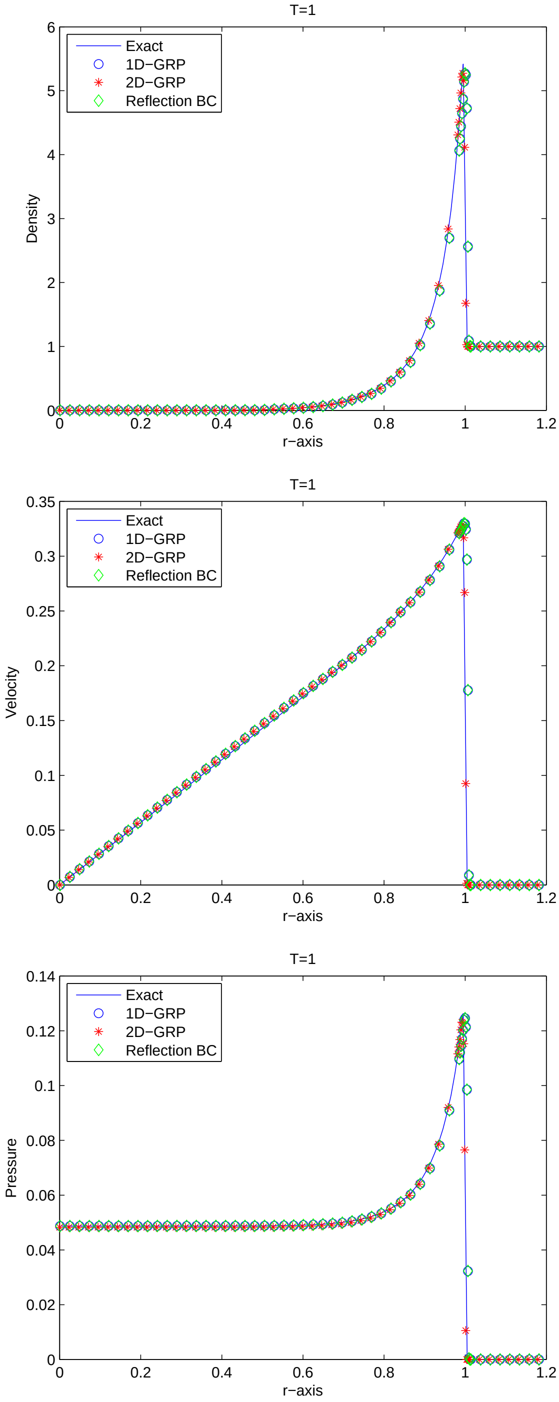

Figure 6: Numerical results for the Sedov-Taylor blast wave problem by the Eulerian GRP scheme: $300\times 20$ grids are used for the two-dimensional case.

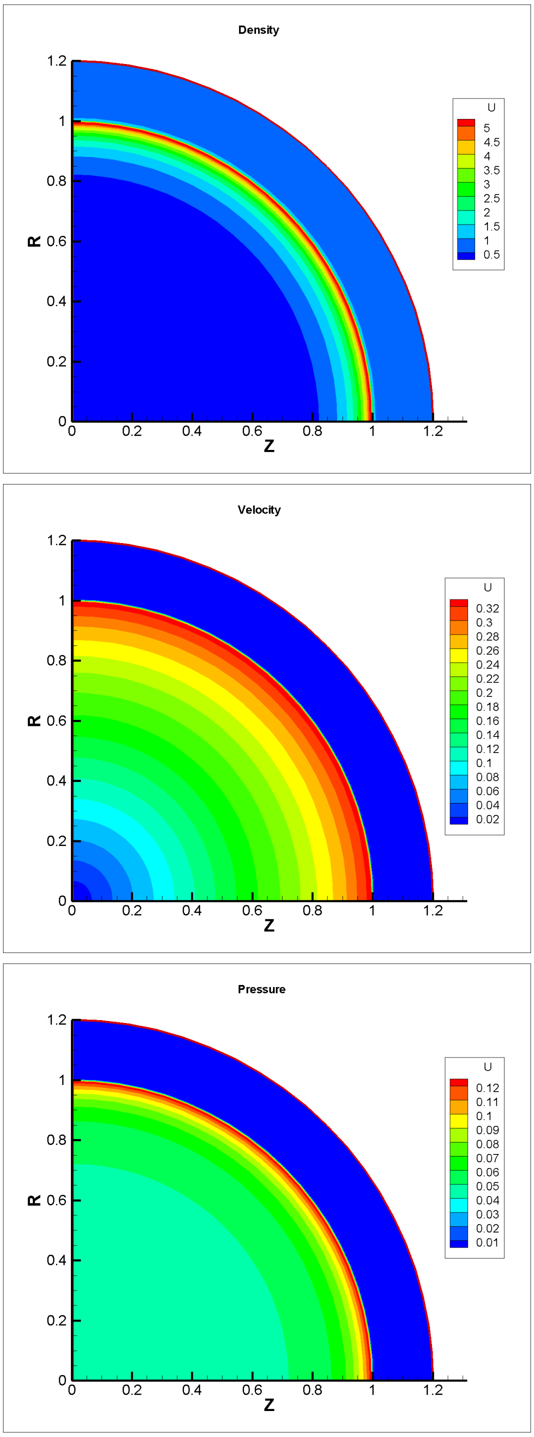

Figure 7: The contour of $\rho$, $u$, $p$ at $T=1$ for the Sedov-Taylor blast wave problem by the Eulerian GRP scheme: $300\times 20$ grids are used.

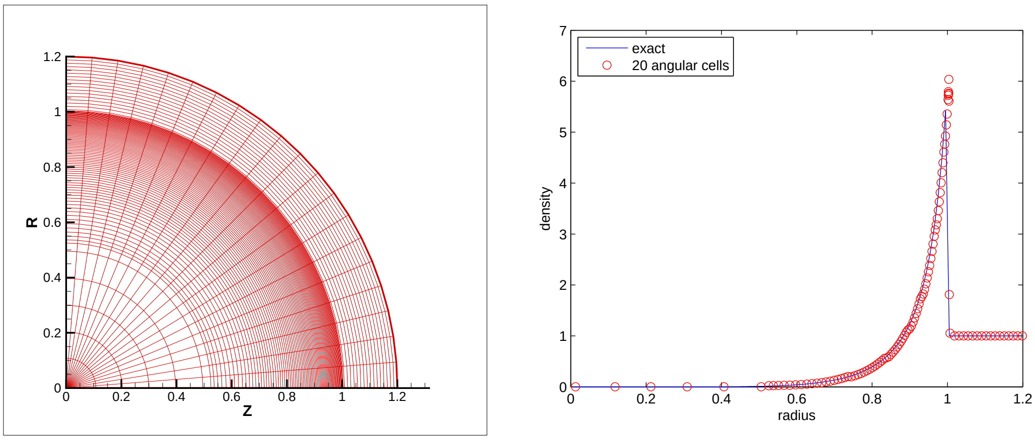

Figure 8: The result of the Sedov-Taylor blast wave problem at $T=1$ by the Lagrangian GRP scheme. Left: final grid with $300\times 20$ cells; Right: exact solution and computational solution for the density.

As shown in Fig. 9, the second shock has formed and is moving inwards to the location about $\xi=6.0$, which matches the numerical results in [24]. It seems that the different boundary conditions at the center are both applicable for this numerical case. The numerical results in Fig. 10 also have the symmetrical property.

We also present the Lagrangian GRP results for this problem. Fig. 11 shows that the grid is symmetrical at $T=15$ and the positions of the shock and the contact discontinuity computed by two-dimensional Lagrangian GRP scheme are quite in agreement with the results computed by the one-dimensional GRP scheme.

## 5.5 A steady flow in a converging-diverging nozzle

Here we adopt the examples in [7] to test the ability of our scheme. The computational domain is $(r,z)\in[0,1]\times[0,1])$ and the cross-sectional area function $A(z)$ is defined as follows,

$$A(z)=\begin{cases} A_{in}\exp(-\ln(A_{in}\sin^2(2\pi z))), & 0\le z\le 0.25,\\ A_{ex}\exp(-\ln(A_{ex}\sin^2(2\pi(1-z)/3))), & 0.25\le z\le 1,\end{cases} \tag{5.8}$$

where $A_{in}=4.8643$ and $A_{ex}=4.2346$. The initial condition is

$$U(r,z,0)=(\rho,u,v,p)(r,z,0)=\begin{cases} (\rho_0,0,0,p_0), & 0<z<0.25,\\ (\rho_0(p_b/p_0)^{1/\gamma},0,0,p_b), & 0.25<z<1,\end{cases} \tag{5.9}$$

where $\rho_0=p_0=1$ and $p_b$ is a constant value determined by the steady state solution at $z=1$.

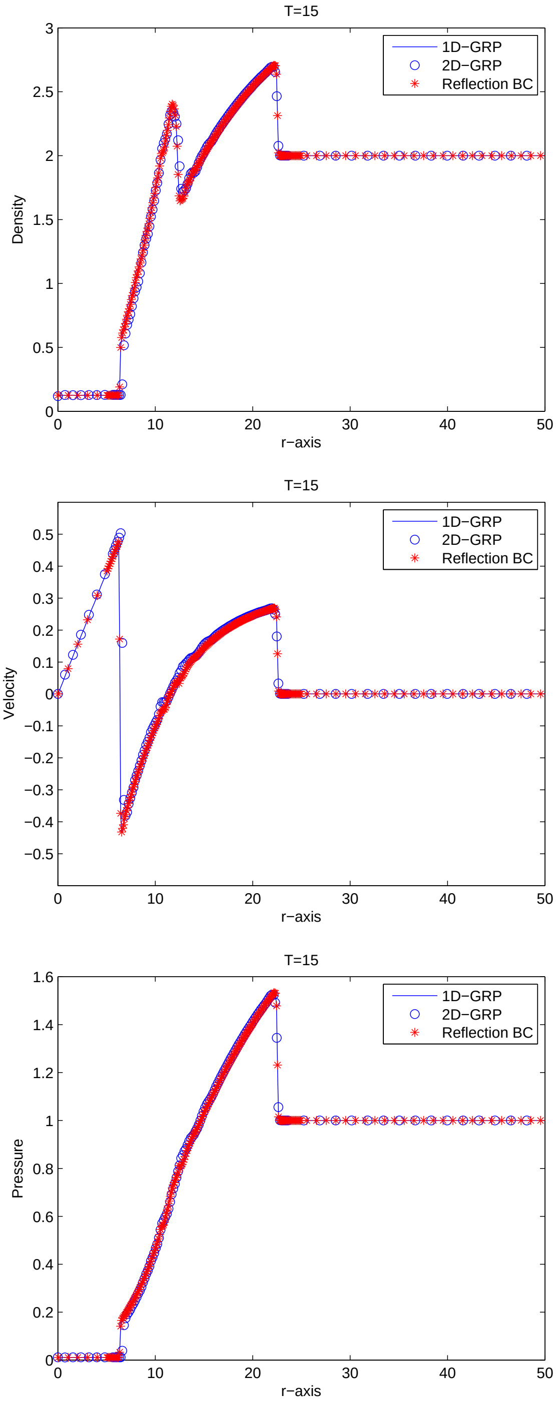

Figure 9: Numerical results for the spherical explosion by the Eulerian GRP scheme: $300\times 20$ grids are used for the two-dimensional case.

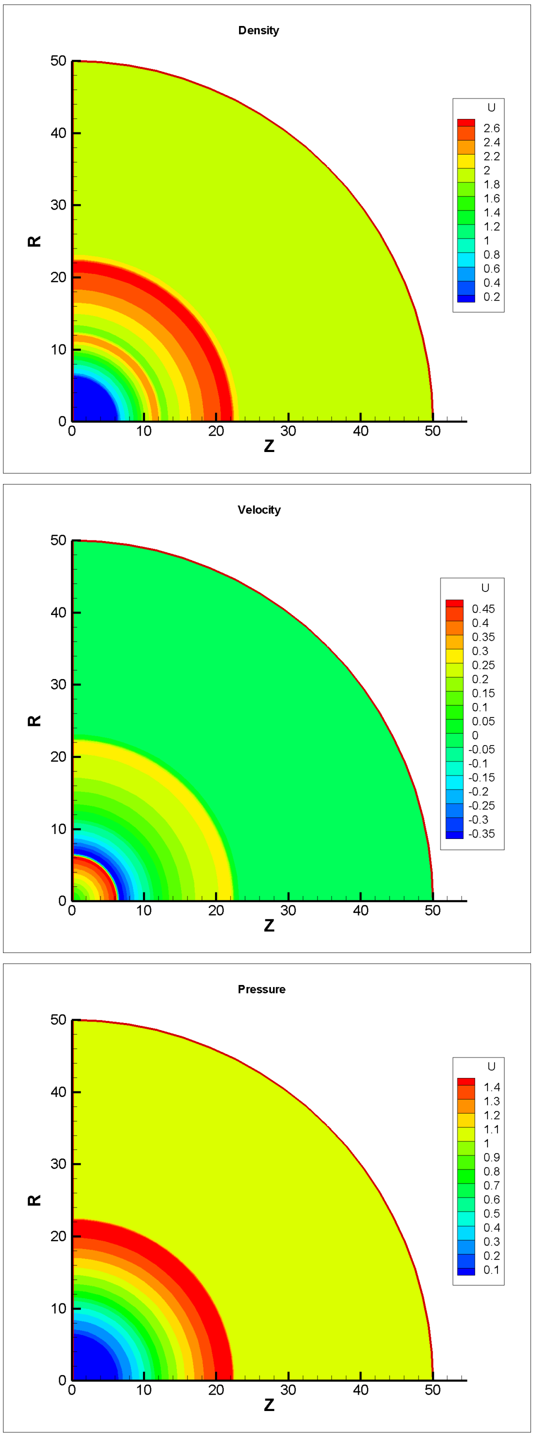

Figure 10: The contour of $\rho$, $u$, $p$ at $T=15$ for the spherical explosion by the Eulerian GRP scheme: $300\times 20$ grids are used.

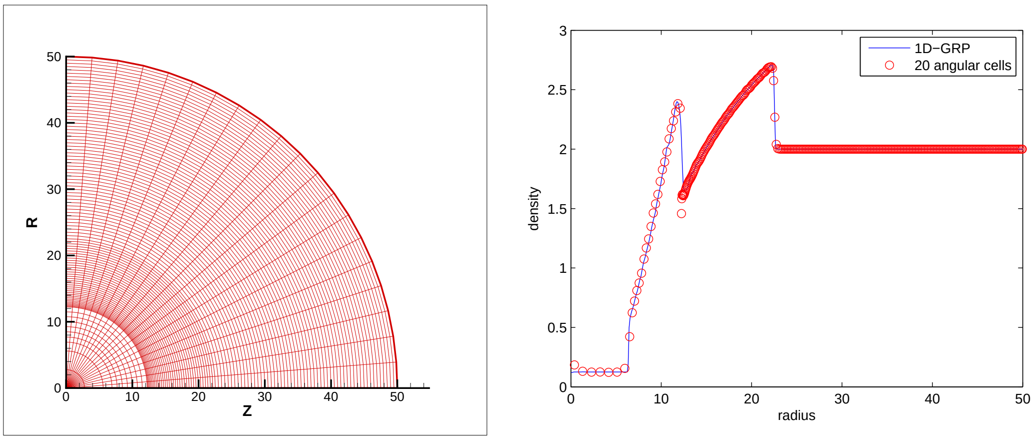

Figure 11: The result of the spherical explosion at $T=15$ by the Lagrangian GRP scheme. Left: final grid with $300\times 20$ cells; Right: 1D GRP solution and computational solution for the density.

The index $\gamma=1.4$ is denoting a perfect gas and the Mach number $M(z)$ is determined by $A(z)$ through the following relation

$$[A(z)]^2=\frac{1}{M^2(z)}\left[\frac{2}{\gamma+1}\left(1+\frac{\gamma-1}{2}M^2(z)\right)\right]^{\frac{\gamma+1}{\gamma-1}}. \tag{5.10}$$

Two cases are considered:

(A) A smooth flow where $p(1)=0.0272237$ and $M(1)=3$.

(B) $p(1)=0.4$ leads to a discontinuous state solution, as shown by the solid line in Fig. 13.

We adopt the same boundary conditions at $z=0$ and 1 proposed in [7]. We use the Eulerian GRP 2D scheme to test the two cases, and we find that our GRP solution is in a quite good agreement with the steady solution. For case (A), its solution is continuous, while for case (B) there exists a shock. Thus different boundary conditions will lead to the different solutions.

## Acknowledgments

Rui Chen is supported by the China Postdoctoral Science Foundation grant No. 2016M591122 and by the Fundamental Research Funds for Central Universities 24820182018RC25-500418780. Jiequan Li is supported by NSFC with No. 11771054 and Foundation of LCP. Baolin Tian is supported by NSFC with No. 11472059 and NSAF with No. U1630247.

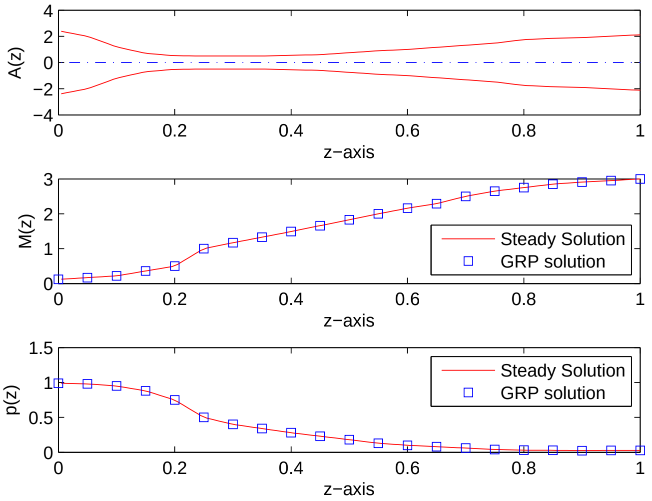

Figure 12: Numerical results for Nozzle Flow problem by the Eulerian GRP scheme at time $t=15.5$: $100\times 20$ grids are used for the two-dimensional case.

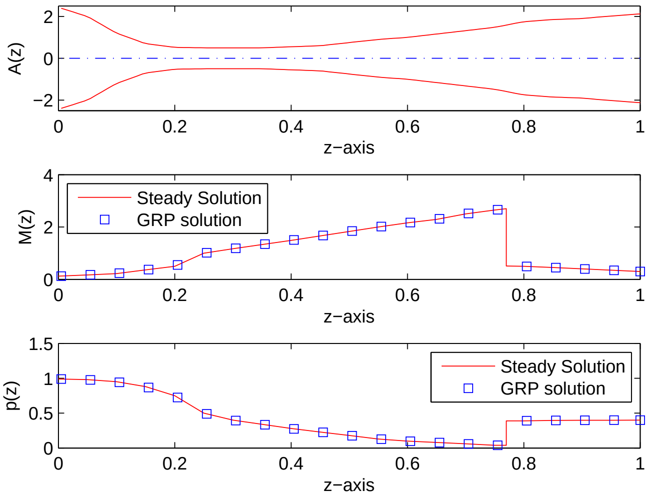

Figure 13: Numerical results for Nozzle Flow problem by the Eulerian GRP scheme at time $t=15.5$: $100\times 20$ grids are used for the two-dimensional case.

## References

[1] R. Abgrall and C.W. Shu, Handbook of numeriacl methods for hyperbolic problems: basic and fundamental issues, Vol. *XVII* in Handbook of Numerical Analysis, North-holland 2016.

[2] B. P. Barber, R. A. Hiller, R. Lofstedt, S. J. Putterman and K. R. Weninger, Defining the Un-

knowns of Sonoluminescence, Phys Reports. 281 (1997), 65–143.

[3] T.Barth, D.C. Jesperson, The design and application of upwind schemes on unstructed meshes, AIAA Report, 89-0366, 1989.

[4] M. Ben-Artzi, A. Birman, Computation of reactive duct flows in external fields, J. Comput. Phys. 86 (1990) 225-255.

[5] M. Ben-Artzi, J. Falcovitzi, A second-order Godunov-type scheme for compressible fluid dynamics, J. Comput. Phys. 55 (1) (1984) 1-32.

[6] M. Ben-Artzi, J. Falcovitz and U. Feldman, Remarks on high-resolution split schemes computation, SIAM J. Sci. Comp. 22(2000), 1008-1015.

[7] M. Ben-Artzi, J. Falcovitzi, Generalized Riemann Problems in Computational Fluid Dynamics, Cambridge University Press, 2003.

[8] M. Ben-Artzi and J. Li, Hyperbolic conservation laws: Riemann invariants and the generalized Riemann problem, Numerische Mathematik, 106, 369–425, 2007.

[9] M. Ben-Artzi, J. Li, G. Warnecke, A direct Eulerian GRP scheme for compressible fluid flows, J. Comput. Phys. 218 (2006) 19-34,

[10] D.W. Boyer, An experimental study of the explosion generated by a pressurized sphere, J. Fluid Mech. 9 (1960) 401-429.

[11] H.L. Brode, Theoretical Solutions of Spherical Shock Tube Blasts, The RAND Corporation, RM-1974, 1957.

[12] P.H. Browmne and K.B. Wallick, The reduction of mesh tangling in two-diensional Lagrangian hydrodynamics codes by the use of viscosity, artificial viscosity, and TTS (Temporary Triangular Subzoning for Long, Thin Zones), Los Alamos Report LA-4740-MS, 1971.

[13] T. Buffard, S. Clain, Monnoslope and multislope MUSCL methods for unstructured meshes, J. Comput. Phys. 229 (2010) 3745-3776.

[14] E.J. Caramana, D.E. Burton, M.J. Shashkov, P.P. Whalen, The construction of compatible hydrodynamics algorithms utlizing conservation of total energy, J. Comput. Phys., 146 (1998) 227-262.

[15] X. Chen, Y. Zhu and C. B. Lee, Interactions between second mode and low-frequency waves in a hypersonic boundary layer. J. Fluid Mech. 820 (2017), 693-735.

[16] J. Cheng, C.-W. Shu, A cell-centered Lagrangian scheme with preservation of symmetry and conservation properties for compressible fluid flows in two-dimensional cylindrical geometry, J. Comput. Phys. 229 (2010) 7191-7206.

[17] J. Cheng, C.-W. Shu, Second order symmetry-preserving conservative Lagrangian scheme for compressible Euler equations in two-dimensional cylindrical coordinates, J. Comput. Phys. 272 (2014), 245–265.

[18] J. Cheng, C.-W. Shu, Positivity-preserving Lagrangian scheme for multi-material compressible flow, J. Comput. Phys. 257 (2014), part A, 143–168.

[19] E. Godlewski, P.-A. Ravilart, Numerical approximation of hyperbolic systems of conservation laws, Applied Mathematical Science, vol. 118, Springer, 1996.

[20] E. Han, J. Li, H. Tang, An daptive GRP scheme for compressible fluid flows, J. Comput. Phys. 229 (2010) 1448-1466.

[21] C. B. Lee, Z. Su, H. J. Zhong, S. Y. Chen, M. D. Zhou and J. Z. Wu, Experimental investigation of freely falling thin disks. Part 2: Transition of three-dimensional motion from zigzag to spiral. J. Fluid Mech. 732 (2013), 77–104.

[22] C. B. Lee and J. Z. Wu, Transition in wall-bounded flows. Appl. Mech. Rev. 61 (2012), 030802.

[23] J. Li, Z. Sun, Remark on the generalized Riemann problem method for compressible fluid flows, J. Comput. Phys. 222 (2007) 796-808.

[24] J. Li, T.G. Liu, Z. Sun, Implementation of the GRP scheme for computing radially symmetric compressible fluid flows, J. Comput. Phys. 228 (2009) 5867-5887.

[25] J. Li, Y. Zhang, The adaptive GRP scheme for compressible fluid flows over unstructured meses, J. Comput. Phys. 242 (2013) 367-386.

[26] T.G. Liu, B.C. Khoo, K.S. Yeo, The numerical simulations of explosion and imposion in air: use of a modified Harten's TVD scheme, Int. J. Numer. Meth. Fluids 31 (1999) 661-680.

[27] P. Maire, B. Nkonga, Multi-scale Godunov-type method for cell-centered discrete Lagrangian hydrodynamics, J. Comput. Phys. 228(3) (2009) 799-821.

[28] P. Maire, A hign-order cell-centered Lagrangian scheme for compressible fluid flows in two-dimensional cylindrical geometry, J. Comput. Phys. 228 (2009) 6882-6915.

[29] D.J. Marvriplis, Revisiting the least-squares procedure for gradient reconstruction on unstructured meshses, AIAA-Paper, pp. 2003-3986, June 2003.

[30] A. Mignone, High-order conservative reconstruction schemes for finite volume methods in cylindrical and spherical coordinates, J. Comput. Phys. 270 (2014), 784–814.

[31] W.F. Noh, Errors for calculations of strong shocks using an artificial viscosity and artificial heat flux, J. Comput. Phys. 72 (1987) 78-120.

[32] M. Omang, S. Borve, J. Trulsen, SPH in spherical and cylindrical coordinates, J. Comput. Phys. 213 (2006) 391-412.

[33] L.I. Sedov, Similarity and Dimensional Methods in Mechanics, Academic Press, New York, 1959.

[34] E.F. Toro, Riemann solvers and Numerical Methods for Fluid Dynamics: a Pratical Introduction, Springer, 1997.

[35] P. V$\acute{a}$chal, B. Wendroff, A symmetry preserving dissipative artificial viscosity in r-z geometry, J. Comput. Phys. 258 (2014) 118-136.

[36] P. V$\acute{a}$chal, B. Wendroff, Symmetry preservation and voluume consistency in an r-z staggered scheme, 11th Word Congress on Computational Mechanics, 2015.